Impacts of Vertical Nonuniform Beam Filling on the Observability of Secondary Ice Production due to Sublimation

JACOB T. CARLIN,[a,b] EDWIN L. DUNNAVAN,[a,b] ALEXANDER V. RYZHKOV,[a,b,c] AND MARIKO OUE[d]

[a] Cooperative Institute for Severe and High-Impact Weather Research and Operations, University of Oklahoma, Norman, Oklahoma
[b] NOAA/OAR/National Severe Storms Laboratory, Norman, Oklahoma
[c] School of Meteorology, University of Oklahoma, Norman, Oklahoma
[d] School of Marine and Atmospheric Sciences, Stony Brook University, State University of New York, Stony Brook, New York

(Manuscript received 12 July 2022, in final form 3 October 2022)

ABSTRACT: Quasi-vertical profiles (QVPs) of polarimetric radar data have emerged as a powerful tool for studying precipitation microphysics. Various studies have found enhancements in specific differential phase K_{dp} in regions of suspected secondary ice production (SIP) due to rime splintering. Similar K_{dp} enhancements have also been found in regions of sublimating snow, another proposed SIP process. This work explores these K_{dp} signatures for two cases of sublimating snow us-ing nearly collocated S- and Ka-band radars. The presence of the signature was inconsistent between the radars, prompting exploration of alternative causes. Idealized simulations are performed using a radar beam-broadening model to explore the impact of nonuniform beam filling (NBF) on the observed reflectivity Z and K_{dp} within the sublimation layer. Rather than an intrinsic increase in ice concentration, the observed K_{dp} enhancements can instead be explained by NBF in the presence of sharp vertical gradients of Z and K_{dp} within the sublimation zone, which results in a K_{dp} bias dipole. The sever-ity of the bias is sensitive to the Z gradient and radar beamwidth and elevation angle, which explains its appearance at only one radar. In addition, differences in scanning strategies and range thresholds during QVP processing can constructively enhance these positive K_{dp} biases by excluding the negative portion of the dipole. These results highlight the need to con-sider NBF effects in regions not traditionally considered (e.g., in pure snow) due to the increased K_{dp} fidelity afforded by QVPs and the subsequent ramifications this has on the observability of sublimational SIP.

SIGNIFICANCE STATEMENT: Many different processes can cause snowflakes to break apart into numerous tiny pieces, including when they evaporate into dry air. Purported evidence of this phenomenon has been seen in data from some weather radars, but we noticed it was not seen in data from others. In this work we use case studies and models to show that this signature may actually be an artifact from the radar beam becoming too big and there being too much variability of the precipitation within it. While this breakup process may actually be occurring in reality, these results suggest we may have trouble observing it with typical weather radars.

KEYWORDS: Snow; Cloud microphysics; Secondary ice production; Sublimation; Radars/Radar observations; Idealized models

1. Introduction

Precipitation microphysics constitute a primary source of uncertainty in the global climate system and its modeling (Zhao et al. 2016; Bodas-Salcedo et al. 2019; Morrison et al. 2020). These uncertainties are protracted by relatively scarce in situ observations and the necessarily simplified treatment of precipitation microphysics in numerical weather prediction models owing to the intractable number of variables and range of spatial scales across which these processes occur. One of the largest known deficiencies in current microphysical parameterization schemes concerns the established observation that ice concentrations often exceed that of available primary ice-nucleating particles by several orders of magnitude. As such, much attention has been devoted to so-called secondary ice production (SIP), where parent ice particles emit small fragments that can rapidly increase ice concentrations and go on to serve as parent ice particles themselves. Multiple SIP mechanisms have been proposed, including rime splintering (Hallett and Mossop 1974), collisional breakup (Phillips et al. 2017), and drop shattering upon freezing (Phillips et al. 2018). For full reviews of proposed SIP mechanisms see Field et al. (2017) and Korolev and Leisner (2020).

Polarimetric weather radars have emerged as a powerful remote sensing tool for studying and characterizing a wide range of precipitation microphysical processes (e.g., Kumjian 2013a,b). A number of recent studies have observed enhanced specific differential phase K_{dp} in regions believed to be experiencing SIP by rime splintering (Grazioli et al. 2015; Sinclair et al. 2016; Kumjian et al. 2016; Kumjian and Lombardo 2017), a primary source of SIP (Hallett and Mossop 1974). In contrast with reflectivity Z and differential reflectivity Z_{DR}, which are dominated by the electromagnetic backscattering amplitudes of the largest hydrometeors, K_{dp}}defined as one-half the range derivative of the differential phase Φ_{DP} between the horizontal and vertical polarization channels}is more sensitive to small, anisotropic hydrometeors (e.g., Ryzhkov et al. 1998), and is thus well-suited

Corresponding author: Jacob T. Carlin, jacob.carlin@noaa.gov

DOI: 10.1175/JTECH-D-22-0076.1

to detect large increases in the concentration of small particles due to SIP in the presence of larger particles.

Carlin et al. (2021) reported similar regions of enhanced K_{dp} within the snow sublimation zone of numerous stratiform precipitation cases. The K_{dp} in these regions often exceeded 0.28 km^{21} at S band and were collocated with sharp gradients of Z and relative humidity with respect to ice (RH_i). Lacking in situ data, the authors conjectured these enhancements were evidence of SIP due to sublimation. While comparatively less studied, sublimational SIP has been observed for individual particles in laboratory studies and was found to occur for sublimating graupel and dendritic crystals (Schaefer and Cheng 1971; Oraltay and Hallett 1989; Dong et al. 1994; Bacon et al. 1998), with fragment emission rates dependent on the shape and size of the parent particle and the ambient temperature and RH_i; plates and columns did not undergo sublimational SIP (Oraltay and Hallett 1989). Korolev and Leisner (2020) questioned the importance of SIP due to sublimation, as the emitted fragments would rapidly sublimate in air dry enough to promote SIP unless they were recirculated into supersaturated regions, but Phillips et al. (2021) challenged this as the continual emission of fragments and their sublimation should result in a quasi equilibrium of enhanced ice concentrations. The scarce observational data on sublimational SIP were synthesized into a parameterization scheme by Deshmukh et al. (2022), who showed equilibrium "ice-enhancement ratios" of 5–10 times the parent ice particle concentrations were possible. Despite this, Patade et al. (2022) found only marginally enhanced K_{dp} when simulating stratiform precipitation with this scheme coupled to a forward polarimetric radar operator (Ryzhkov et al. 2011), although such calculations are sensitive to the presumed size, shape, and density of the emitted fragments.

In the time since it was first reported in Carlin et al. (2021), the authors noted that the proposed sublimational SIP K_{dp} signature was not observed at other research radars they examined. Absent any comprehensive in situ observations from naturally occurring sublimation events to help contextualize the radar signatures, this study seeks to further explore the possible causes of the observed K_{dp} enhancements in sublimation regions by considering an alternate hypothesis: that data quality issues pertaining to nonuniform beam filling (NBF) may instead be responsible. To accomplish this, multifrequency data from independent operational and research radars for two sublimation events observed in southeastern New York are explored to further investigate the sublimational SIP hypotheses of Carlin et al. (2021) in section 2, and simulations employing a beam-broadening model to study the impacts of NBF on the observed K_{dp} are performed in section 3. A summary and discussion of the implications of these findings for the observability of sublimational SIP using the NEXRAD WSR-88D network are discussed in section 4.

2. Radar observations of potential sublimational SIP

a. KOKX and KASPR details

This study uses data from two radars: The NEXRAD WSR-88D network KOKX radar site in Upton, New York, and the Stony Brook University Ka-band Scanning Polarimetric cloud Radar (KASPR; Kollias and Oue 2020) in Stony Brook, New York. KOKX collects PPI scans at various elevation angles depending on the volume coverage pattern (VCP) selected depending on operational forecasters' contemporaneous needs. In this study, two VCPs are included: the so-called clear-air mode VCP 32 (with 5 elevation angles ranging from approximately 0.58 to 4.58 every 1.08 and volume scans completed every ′ 1 0 min), and a "precipitation mode" VCP 215 (with 15 elevation angles ranging from approximately 0.58 to 19.58 and volume scans completed every ′ 6 min). WSR-88D radars will often use VCP 32 when precipitation is far from the radar, the precipitation is evolving slowly, and/or Z values are low, and hence it is often in place during the gradual onset of snow during sublimation events before switching over to a precipitation-mode VCP. Therefore, WSR-88D radars will observe regions of strong sublimation predominantly with low elevation angles. In contrast, KASPR operates as a research radar with three separate scanning strategies: A vertically pointing (VPT) mode, a PPI mode, and a range–height indicator (RHI) mode. This study uses KASPR data exclusively from the VPT and PPI scans. In particular, all KASPR PPI scans are performed with a fixed elevation angle of 158. Unlike the WSR-88D radars which simultaneously transmit and receive horizontally and vertically polarized waves (SHV mode), KASPR is "fully polarimetric" which allows for the additional computation of linear depolarization ratio (LDR) and other cross-polarimetric variables. Additional details of each radar are provided in Table 1.

Figure 1 shows the locations of KOKX and KASPR as well as their PPI ranges for two constant heights AGL. The radars are very close to one another (22.4 km separation distance) which allows for overlap of their viewing domains even at a height of 2.0 km and the typical highest elevation angle. This overlap in sampling volumes between KOKX and KASPR at low levels is important for comparing apparent sublimational radar signatures occurring within the lowest few km of the atmosphere. Unlike KOKX, the VPT scanning mode of KASPR additionally allows for investigation of possible sublimational SIP signatures using Doppler power and LDR spectra. Previous studies have used the presence of bimodal VPT Doppler power spectra as a way to infer the existence of multiple distinct particle populations, such as the coexistence of ice and supercooled liquid water (e.g., Zawadzki et al. 2001; Li et al. 2021) or parent ice particles and fragments produced by SIP (e.g., Zawadzki et al. 2001; Oue et al. 2015), as SIP frag-ments are expected to have much slower fall speeds than their parent particles. With no supercooled liquid water expected in subsaturated regions, a lack of bimodality in the Doppler spectra within observed sublimation regions can help rule out the possibility of sublimational SIP causing any K_{dp} enhancement. Additionally, LDR is a power-weighted quantity that is related to particle density, nonsphericity, and orientation, with denser, nonspherical canted particles exhibiting enhanced LDR values [e.g., Eq. (5.40) of Ryzhkov and Zrnić 2019; Kumjian et al. 2020]. As such, LDR spectra are useful for identifying the presence of prolate ice columns, which fall in the slow part of the Doppler spectrum and feature distinctly high LDR values near 215 dB (e.g., Oue et al. 2015; Li and Moisseev 2020;

TABLE 1. KOKX and KASPR radar attributes.

Variable	KOKX	KASPR
Latitude	40.86568N	40.89028N
Longitude	272.86398E	273.12808E
Altitude	56 m MSL	48 m MSL
Wavelength	l_{KOKX} 5 10.43 cm	l_{KASPR} 5 0.849 cm
Peak transmit power	700 kW	2.2 kW typical
Pulse repetition frequency (PRF)	Short: 318–1304 Hz; long: 318–452 Hz	Staggered PRF: max 15 kHz
Pulse width	1.57–4.71 mm	0.1–13 mm
Range resolution	250 m	15–200 m
Elevation scanning angles	0.58–19.58, VCP dependent	15.08
Antenna diameter	8.53 m	1.8 m
Antenna gain	45.5 dB	53.3 dB
Antenna beamwidth	1.08	0.328
Cross-polarization isolation	}	227 dB

Li et al. 2021), much higher than the LDR of low-density snow aggregates and oblate spheroidal plates.

To compare the KOKX and KASPR observations, we transform PPI data from each radar into quasi-vertical profiles (QVPs; Ryzhkov et al. 2016). QVPs are azimuthal averages of the PPI scans at a particular elevation angle and displayed as a function of height derived from range. We calculate the corresponding heights of each elevation angle assuming standard atmospheric refraction. Because KASPR and KOKX are at comparable altitudes of 48 and 56 m MSL, respectively, all subsequent radar beam heights are with respect to radar level. To minimize the production of unrepresentative profiles, data were excluded from each QVP profile if fewer than 10% of the gates at a given elevation angle and range had valid data. When multiple elevation angles are available, such as from KOKX, each individual QVP can be interpolated onto a common height grid and further averaged into range-defined quasi-vertical profiles (RDQVP; Tobin and Kumjian 2017). The use of multiple elevation angles allows more data to be used for each RDQVP profile. Because RDQVPs use multiple QVP elevation angles, the height of each QVP corresponds to a different range. To try to limit the data to be most representative of near the radar site, RDQVPs impose a range threshold past which the weights given to each QVP drop off exponentially (often 50 km; Tobin and Kumjian 2017). This distance weighting function is important when considering how radar elevation angles can affect RDQVP profiles. RDQVPs that use larger distance thresholds will naturally incorporate more data from lower elevation angle QVPs than smaller distance thresholds. Unless otherwise stated, all KOKX RDQVPs in this study use a 25-km range threshold.

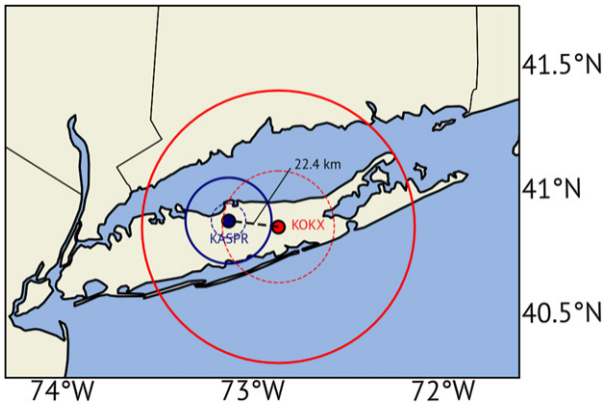

FIG. 1. Map displaying the locations of KOKX and KASPR. Range rings are included for heights of 5 km AGL (solid) and 2 km AGL (dashed) at what is often the highest elevation angle available (15.08 at KASPR, 4.58 at KOKX when in clear-air mode).

KASPR K_{dp} is calculated using the iterative approach of Hubbert and Bringi (1995), with processing details provided in Oue et al. (2018). KOKX K_{dp} is calculated according to Vulpiani et al. (2012, 2015) using the Py-ART radar processing package (Helmus and Collis 2016). To help with noise reduction, we exclude gates with Z , 215 dBZ or r_{hv} , 0.9 and included prefiltering of the F_{DP} field by removing stretches of data with fewer than 5 consecutive valid gates and applying a 7-gate median filter to each F_{DP} profile (i.e., the default Py-ART F_{DP} prefiltering parameters). Based on the findings of Reimel and Kumjian (2021) and knowledge that K_{dp} peaks in snow are generally wide and low amplitude compared to those in convective rain, we chose a 12-gate processing window with 11 iterations. Sensitivity to the number of iterations was found to be quite low, and the 12-gate window was deemed sufficient for retaining minor peaks while having sufficient data for an accurate calculation. Even with these considerations, some amount of uncertainty remains regarding the absolute values of K_{dp} in regions of such low intrinsic values where relative errors may be large; the optimal technique and parameters for calculating K_{dp} in snow deserve further exploration. As shown in Ryzhkov et al. (2011), K_{dp} in the Rayleigh scattering regime is inversely proportional to l. Therefore, throughout this study we scale the KASPR K_{dp} by l_{KASPR}/l_{KOKX} (i.e., compute an equivalent S-band K_{dp} estimate) in order to more easily compare it with the KOKX K_{dp}. No attenuation correction or Z_{DR} bias correction is performed, nor are any adjustments made to Z_{DR} and K_{dp} to account for the radar elevation angle; these impacts are minimal at the elevation angles examined herein (Ryzhkov et al. 1998, 2016; Griffin et al. 2018).

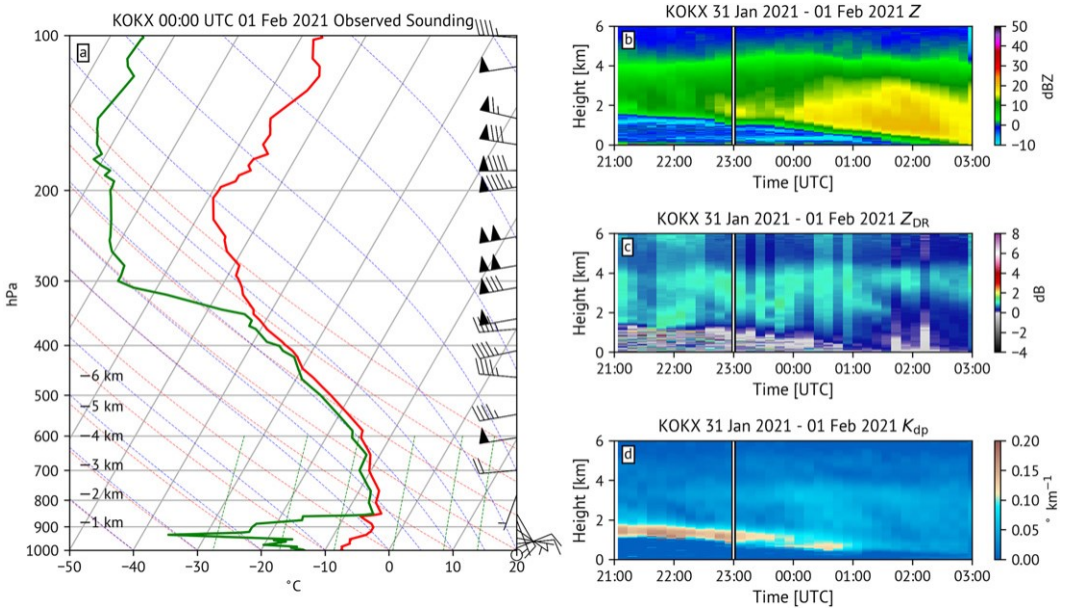

FIG. 2. (a) Observed sounding from KOKX nominally at 0000 UTC 1 Feb 2021 (plotted using MetPy; May et al. 2022). (b)–(d) RDQVPs of (b) Z, (c) Z_{DR}, and (d) K_{dp} from KOKX using a 25-km averaging radius. The vertical line in (b)–(d) denotes the approximate sounding launch time.

b. Cases

To find suitable cases of sublimation to examine, we searched the KOKX sounding archive for cases during the KASPR observing period (i.e., December–February during the 2019/20 and 2020/21 winter seasons) that indicated a layer of substantially dry air underlying a deep, precipitation-generating saturated layer. KASPR data were collected as part of the Investigation of Microphysics and Precipitation for Atlantic Coast-Threatening Snowstorms (IMPACTS) campaign (McMurdie et al. 2022). Two cases were selected that had KASPR data available for the duration of the sublimation period prior to snow reaching the surface: 31 January–1 February 2021 ("Case 1") and 12–13 February 2020 ("Case 2").

1) CASE 1: 31 JANUARY–1 FEBRUARY 2021

The first period we examine is from 2100 UTC 31 January 2021 to 0300 UTC the following day. This case is characterized by a low-level dry air mass where strong sublimation moistens the environment (cf. Carlin et al. 2021) until precipitation reaches the surface around 0300 UTC 1 February 2021. Figure 2a shows the nominal 0000 UTC 1 February 2021 sounding (with a launch time of approximately 2300 UTC 31 January 2021) from the KOKX site. A deep saturated layer exists up to 350 hPa that overlays a layer of dry air, where dewpoint depressions maximize at ′308C within the lowest 1.0 km MSL. Figures 2b, 2c, and 2d show the corresponding KOKX RDQVP time–height plots during this period. The Z field is initially elevated as snow sublimates below 2 km. This layer gradually descends toward the surface as the dry air underlying this precipitation is progressively moistened. In concert with this Z gradient, Fig. 2d shows a coherent layer of enhanced K_{dp} around the top of the sublimation layer with maximal values approaching 0.28 km^{21} that descends with the sublimation zone until approximately 0100 UTC. Elevated values of Z_{DR} and Z above this K_{dp} enhancement indicate the presence of small to moderately sized, anisotropic ice particles. With the exception of the very end of the 2100–0300 UTC period, KOKX was operating in VCP 32 (clear-air mode).

Figure 3 shows PPI scans of Z, F_{DP}, and K_{dp} at the 4.58 elevation angle from KOKX and additionally LDR from KASPR at approximately 2200 UTC 31 January 2021, as well as the corresponding QVPs. While the QVPs shown in Fig. 3 include all azimuths, an examination of the KOKX sector average over the approximate KASPR domain showed nearly indistinguishable results, highlighting the high degree of homogeneity in the precipitation field. The Z profiles between both radars are quite consistent (Figs. 3a–c), with Z increasing to 10 dBZ just below 2 km before rapidly decreasing to less than 210 dBZ within a ′250-m-deep layer. However, there are noticeable discrepancies between KOKX and KASPR for F_{DP} and K_{dp}. While the (scaled) KASPR K_{dp} profile is relatively constant and ranges from approximately 08–0.058 km^{21} throughout the entire precipitation layer, the KOKX K_{dp} profile clearly exhibits a very large K_{dp} peak well above 0.18 km^{21} within the sublimation region (Fig. 3i) that is quite concentric and occurs at most azimuths (Fig. 3g). This K_{dp} discrepancy between KOKX and KASPR is quite suspicious considering the close proximity of KOKX and KASPR (Fig. 1). The lack of enhancement in the KASPR data also cannot be attributed to its more oblique viewing angle of oblate spheroidal par-ticles; K_{dp} should be diminished by only 7% compared to a broadside viewing angle [see Eq. (2) of Griffin et al. 2018]. This K_{dp} enhancement also does not appear to be due to the

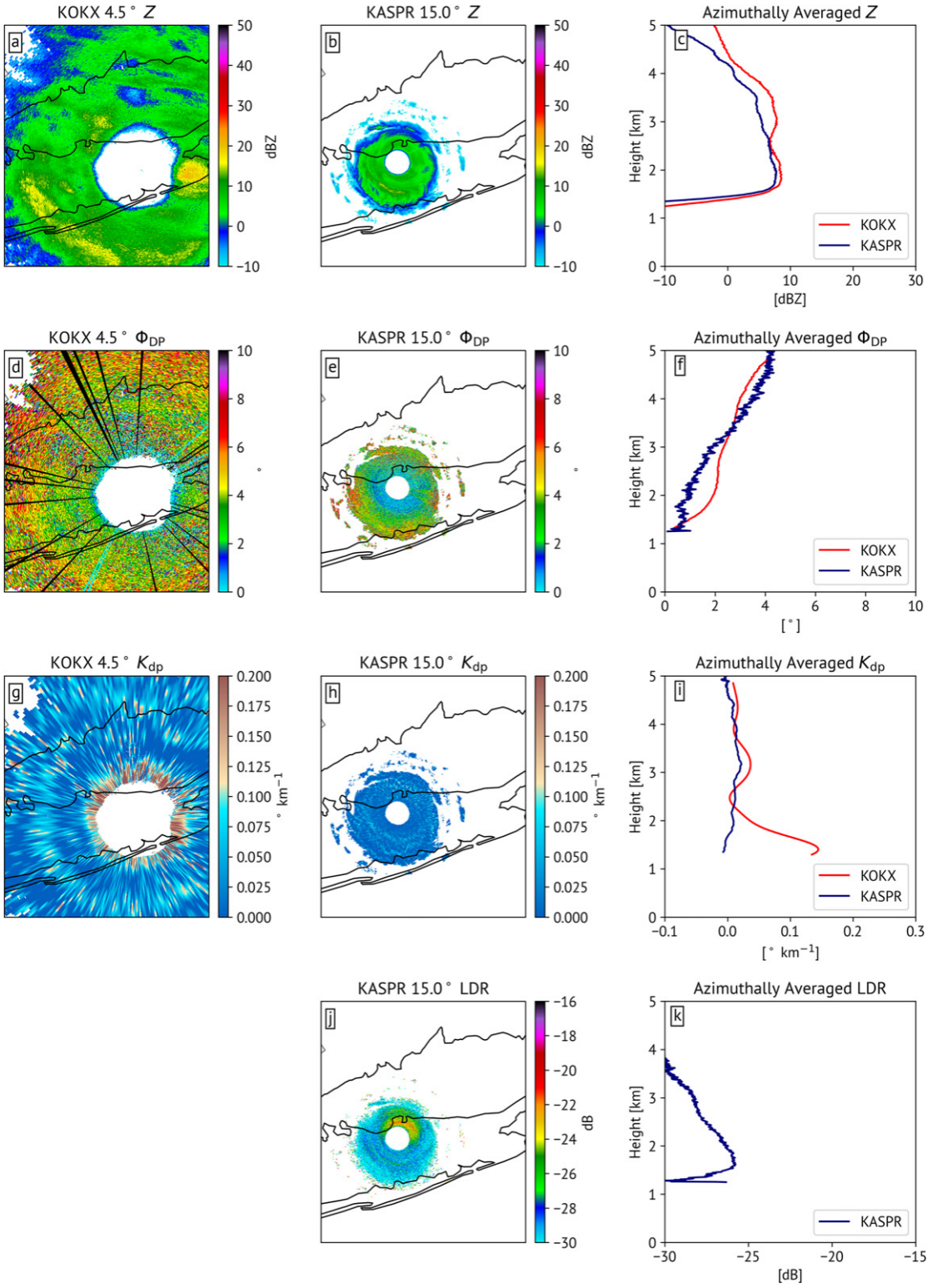

FIG. 3. PPIs of (a),(b) Z, (d),(e) F_{DP}, (g),(h) K_{dp}, and (j) LDR from (a),(d),(g) KOKX from 2207:08 UTC 31 Jan 2021 at the 4.58 elevation angle and (b),(e),(h),(j) KASPR from 2201:34 UTC 31 Jan 2021 at the 15.08 elevation angle. (c),(f),(i),(k) Azi-muthal averages as a function of height from each radar are shown. KASPR K_{dp} in (h) and (i) has been scaled by a factor of I_{KASPR}/I_{KOKX} and KOKX (KASPR) F_{DP} has been shifted by 2568 (268) for a normalized comparison.

K_{dp} processing method or data boundary effects, as a clear increase in the raw F_{DP} values is apparent at KOKX (Figs. 3d,f). LDR values at KASPR are low and remain below 225 dB, typical of snow aggregates (Kumjian et al. 2020), which likely dominate the overall LDR signal in the Rayleigh scattering regime. A small region of locally enhanced LDR is seen to the northeast of the radar with values up to 222 dB (Fig. 3j). However, this is immediately above, rather than within, the sublimation layer, and with no enhancement in K_{dp} accompanying this modest increase in LDR it is unlikely that this signature indicates appreciable sublimational SIP.

Figure 4 shows mean KASPR VPT spectral data for two separate time periods during Case 1. The RH_i was calculated from the observed sounding using the equations for saturation vapor pressure with respect to water and ice provided by Buck (1981, 1996). Interestingly, there is a bimodal spectra apparent at 2208 UTC above the sublimation layer (′1.5–2.5 km AGL; Fig. 4a), with a secondary mode centered around 20.4 m s^{21}. However, the spectral LDR remains very low across both modes and near the detection limit of KASPR (228 to 230 dB; Fig. 4b), making it unlikely this represents a distinct population of column-like crystals. Within the sublimation layer, the spectra is unimodal, with Doppler velocities that rapidly increase as particles sublimate and their terminal velocities decrease. An hour later, the spectra is unimodal through its depth, with the addition of a layer with broadened Doppler spectra and rapidly changing velocities near the top of the sublimation layer (Fig. 4c). These type of rapid changes of Doppler velocity with height are likely explained by turbulence generated from diabatic cooling in the sublimation layer (e.g., Kudo 2013). The LDR at this time show enhanced LDR values up to 220 dB for the faster-falling velocity bins entering the sublimation layer. These fall speeds and LDR values may be indicative of an increase in density due to riming, or simply the existence of large aggregates with diameters greater than 10 mm, which the scattering calculations of Tyynelä et al. (2011) show can produce values of LDR . 220 dB at Ka band. Additionally, the enhanced LDR at the edges of the spectra in Figs. 4b and 4d are due to low SNR and the contribution of noise spectral density at very low values of copolar spectral power. Regardless, within the sublimation layer, an increase in the Doppler velocities, a narrowing and weakening of the unimodal spectra, and values of LDR well below those of column-like crystals suggest no indication of SIP within the sublimation layer. Other time periods (not shown) also do not indicate bimodal Doppler spectra in the sublimation layer.

2) CASE 2: 12–13 FEBRUARY 2020

Unlike Case 1, Case 2 does not exhibit a consistent layer of enhanced K_{dp} within the sublimation layer but does have two K_{dp} enhancement periods at approximately 2200 UTC 12 February and 0000 and 0045 UTC 13 February 2020 (Fig. 5d). The low-level air for this case is even drier than in Case 1, with dewpoint depressions maximizing at more than 408C. Also, the height of the sublimation layer for the shown period is higher than Case 1, beginning at approximately 3.0 km above radar level (ARL) and descending to 2.0 km ARL by 0030–0100 UTC. The brief period of enhanced Z and Z_{DR} at 0130 UTC is due to the intrusion of the melting layer. During this period, KOKX was operating in VCP 215 (precipitation mode).

Figure 6 shows the corresponding 5.08 PPIs and QVPs at approximately 0050 UTC. While VCP 215 includes higher elevation angles, the 5.08 elevation scan is shown for consistency with Fig. 3. The decrease of Z through the sublimation layer is a bit more gradual for this case than Case 1, occurring over a ′500-m-deep layer, although initial values at the top of the sublimation layer were larger (20 dBZ compared to 10 dBZ; Fig. 6c). However, similar to Fig. 3i, Fig. 6i shows a K_{dp} peak at the top of the sublimation layer for KOKX but no such enhancement for KASPR, although it is less azimuthally homogeneous than Case 1 (Fig. 3g). As in Case 1, this is visually apparent even in the raw F_{DP} QVP (Fig. 6f). This behavior is consistent in the Doppler spectra as well, where there is an apparent turbulent layer around 2.0–2.3 km and a subsequent rapid decrease in the unimodal Doppler velocities (Fig. 7a) and no marked increase in the LDR in the slower-falling velocity bins (Fig. 4b). For this case, 0045:47 UTC was the earliest spectra data available from KASPR; the apparent sublimation zone in the Doppler spectra is well below the strong RH_i gradient because the sounding was launched roughly 2 h previous before additional moistening had occurred.

Figures 2 and 5 confirm that KOKX observes K_{dp} enhancements for both of these cases, consistent with the sublimation RDQVPs of Carlin et al. (2021), whereas KASPR does not show these enhancements. Moreover, KASPR spectra are not bimodal in the sublimation region (Figs. 4 and 7) unlike what might be expected if the associated K_{dp} enhancements resulted from appreciable SIP processes, nor does the examined spectral LDR data support the existence of dense, anisotropic, canted particles resulting from SIP within the sublimation layer. Instead, we now explore a different hypothesis: that the emergence of the KOKX K_{dp} signal is instead a result of NBF.

Figure 8 shows an example set of the QVPs that comprise the RDQVPs in Figs. 2 and 5. The time chosen for Case 2 matches the PPIs shown in Fig. 6, while the time chosen for Case 1 coincides with the radiosonde launch and the spectral data shown in Fig. 4b. When viewed separately at each individual elevation angle, the effects of beam broadening in the KOKX data are apparent and pronounced. While there is good agreement with the maximum Z value entering the sublimation layer, which is known with high confidence from the KASPR VPT scans, the Z gradients within the sublimation layer from KOKX become progressively less sharp at lower elevation angles and appear increasingly far below where they are actually located (Figs. 8a,d). This is especially obvious for Case 2 (Fig. 8d), where the sublimation-layer Z gradient measured at low elevation angles appears up to ′1.0 km below the gradient height indicated by the VPT data. These effects become more muted for sublimation regions at lower altitudes (e.g., Fig. 8a). The attendant profiles of F_{DP} and K_{dp} also exhibit interesting characteristics. The F_{DP} profiles reveal a relatively large increase at low levels, followed by a lessening of the slope before assuming a near-constant slope above

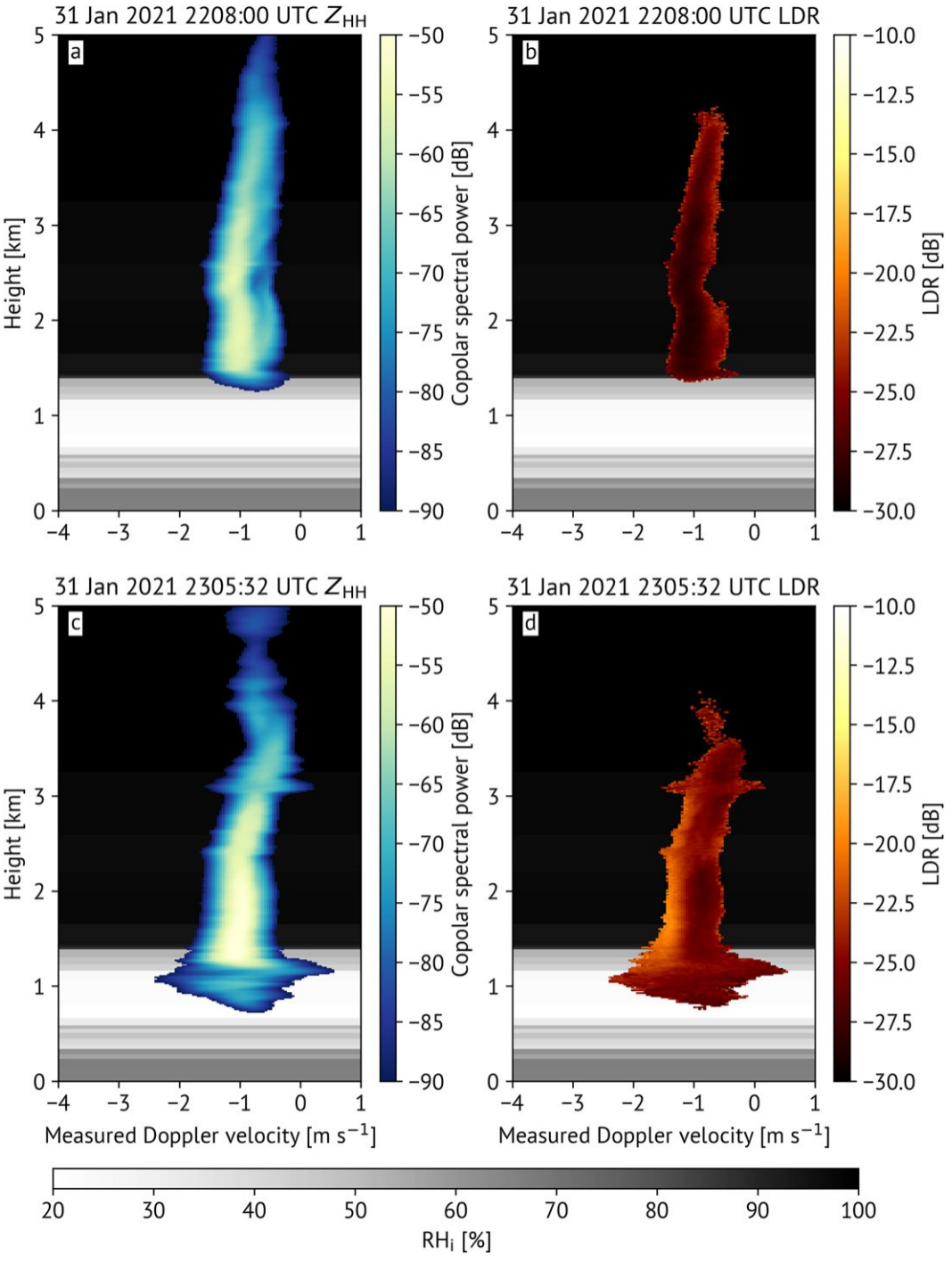

FIG. 4. (a),(c) Copolar spectral power (dB; blue shading) and (b),(d) LDR (dB; red shading) from zenith-pointing KASPR scans at (top) 2208:00 and (bottom) 2305:32 UTC 31 Jan 2021. The corresponding RH_i profile from the 0000 UTC 1 Feb 2021 KOKX sounding is shown in all panels in gray shading. Doppler velocities are defined with negative being downward and LDR is calculated where Z_{HH} . 270 dBm and Z_{VH} . 287 dBm.

the sublimation layer. This is reflected in K_{dp} as a localized peak within the sublimation layer, as discussed in section 2b, above which there is very good correspondence between the KASPR and KOKX K_{dp}. While the K_{dp} enhancement in the mean is quite coherent (e.g., Figs. 2 and 5), it is clear that the height of the K_{dp} enhancement within the sublimation layer increases with elevation angle when viewed separately, with gradually smaller peak magnitudes at higher elevation

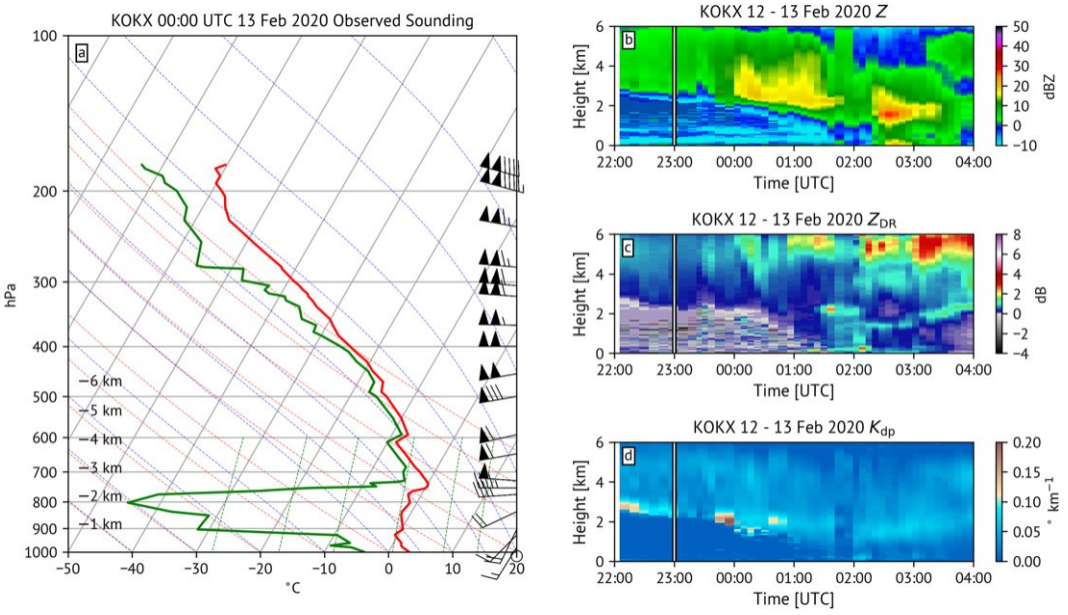

FIG. 5. As in Fig. 2, but for 12–13 Feb 2020.

angles. These observations serve as the basis for initializing and validating the model presented in section 3.

3. Idealized beam-broadening model simulations

To investigate whether NBF can explain the observed discrepancy in K_{dp} between KOKX and KASPR, we attempt to realistically simulate the KOKX observations by incorporating the effects of beam broadening and subsequent NBF using an adaptation of the Ryzhkov and Zrnić (1998) beam-broadening model. This model operates on so-called intrinsic profiles (abbreviated with the subscript "int") of Z, F_{DP}, and K_{dp}, which represent what would be observed with a theoretically perfect radar (e.g., no calibration errors, an infinite number of samples) with an infinitely narrow beamwidth, and produces so-called observed profiles (abbreviated with the subscript "obs") that would be measured by a realistic, imperfect radar when taking the impact of beam broadening on the intrinsic profiles into account. The observed differential phase measured by a radar, $F_{DP,obs}$, can be fundamentally expressed as [Ryzhkov 2007, adapted from their Eq. (A13)]

$$F_{DP,obs} = \arg \int_V Z_{int} Z_{dr,int}^{21/2} |r_{hv,int}| \exp[22(A_h + A_v)] \times \exp[j(F_{DP,int} + d_{int})] I(u,c)\, dr\, du\, dc, \quad (1)$$

where Z_{int} and $Z_{dr,int}$ are the intrinsic reflectivity at horizontal polarization and differential reflectivity in linear units, respectively, $|r_{hv,int}|$ is the magnitude of the intrinsic cross-correlation coefficient, $A_{h,v}$ is the attenuation at horizontal and vertical polarizations, $F_{DP,int}$ is the intrinsic differential phase upon propagation, d_{int} is the intrinsic backscatter differential phase, $I(u, c)$ is the beam illumination function, and the integral is evaluated for the radar resolution volume V in range (r), azimuth (u), and elevation (c). Following Ryzhkov and Zrnić (1998), we make a number of simplifying assumptions: 1) that $Z_{dr,int}$ is close to 1 (in linear units) and does not vary appreciably within the radar resolution volume, 2) that $r_{hv,int}$ is close to 1 and does not vary appreciably within the radar resolution volume, that 3) attenuation and 4) d_{int} are negligible, 5) that the change in the range direction within the radar resolution volume is negligible, and by 6) assuming azimuthal homogeneity. Assumptions 1–4 are based on observed characteristics of dry aggregated snow above and within the sublimation layer (e.g., Carlin et al. 2021), and assumption 5 is predicated on the fact that the range resolution (e.g., 250 m) is much smaller than the resolution in the transverse direction (i.e., in azimuth and elevation). Assumption 6 is also based on the observed characteristics of sublimating snow [i.e., the "donuts" on radar discussed in Carlin et al. (2021) and seen in Figs. 3 and 6] and is used for both Z_{int} and $F_{DP,int}$; this is a conservative assumption that will underestimate the broadening of azimuthally averaged profiles in the vertical, such as QVPs. With these assumptions, Eq. (1) can be expressed as

$$F_{DP,obs}(r, c_0) = \arg \int Z_{int}(r, c) I(c, c_0) \exp[jF_{DP,int}(r, c)]\, dc, \quad (2)$$

where c_0 is the elevation angle at the center of the beam. Similarly, the observed reflectivity Z_{obs} is found according to

$$Z_{obs}(r, c_0) = \int Z_{int}(r, c) I(c, c_0)\, dc: \quad (3)$$

In Eqs. (2) and (3), the integrals are calculated using Simpson's rule, and $I(c, c_0)$ is approximated by an axisymmetric Gaussian two-way antenna pattern (Doviak and Zrnić 1993):

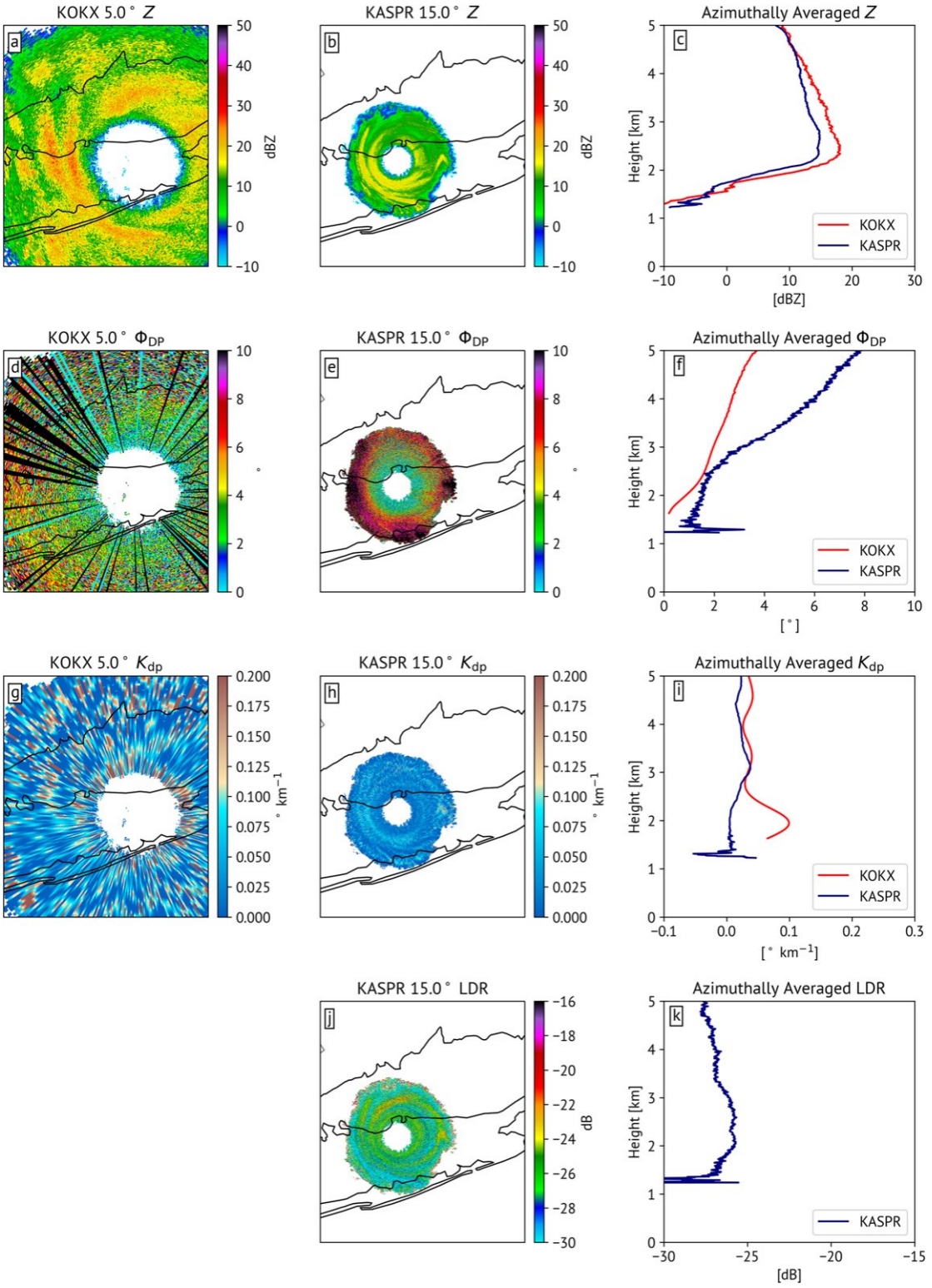

FIG. 6. As in Fig. 3, but for KOKX from 0050:00 UTC 13 Feb 2020 at the 5.08 elevation angle and KASPR from 0050:08 UTC 13 Feb 2020 at the 15.08 elevation angle. KASPR K_{dp} in (h) and (i) has been scaled by a factor of I_{KASPR}/I_{KOKX} and KOKX (KASPR) F_{DP} in has been shifted by 2628 (128) for a normalized comparison.

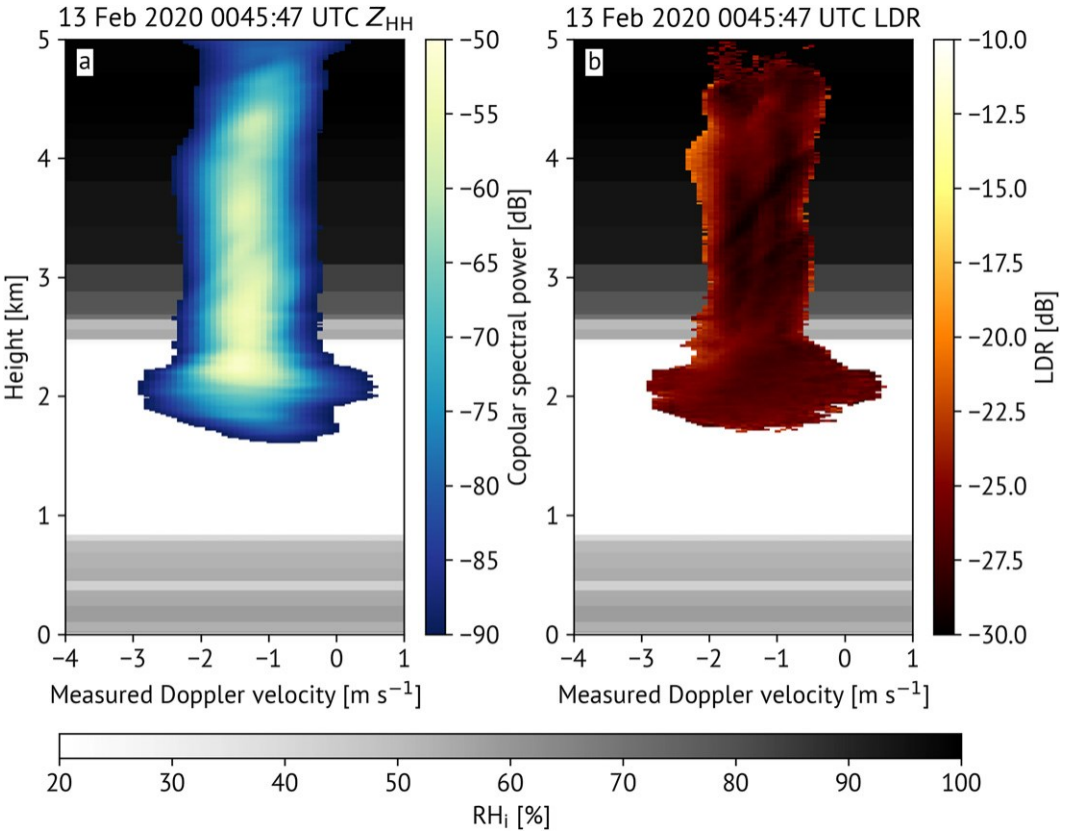

FIG. 7. As in Fig. 4, but for 0045:47 UTC 13 Feb 2020 and with the corresponding RH_i profile from the 0000 UTC 13 Feb 2020 KOKX sounding (gray shading). LDR is calculated where Z_{HH} . 270 dBm and Z_{VH} . 290 dBm.

$$I(c, c_0) = \frac{1}{2ps^2}\exp\left[-\frac{1}{2}\left(\frac{c - c_0}{s}\right)^2\right], \quad (4)$$

where $s = V/4\ln(2)$ and V is the one-way 3-dB antenna beamwidth following Ryzhkov (2007). We define V to be 1.08 to emulate the WSR-88D beam pattern (Table 1). Because we assume the precipitation is azimuthally homogeneous, we prescribe uniform intrinsic profiles of Z_{int} and $K_{dp,int}$ that characterize a slab of precipitation of infinite length over the radar site. Then, for each simulated radar gate at range r we calculate the heights that all points within $I(c, c_0)$ intersect the intrinsic profiles. The $\Phi_{DP,int}$ at r along each elevation angle within $I(c, c_0)$ is found by integrating the $K_{dp,int}$ along the ray according to

$$\Phi_{DP,int}(r, c) = 2\int_{r50}^{r} K_{dp,int}(r)dr: \quad (5)$$

Here, a Δr of 250 m is used to mimic the NEXRAD range gate spacing. We then integrate across $I(c, c_0)$ to find $\Phi_{DP,obs}$ and $Z_{h,obs}$ centered at c_0 according to Eqs. (2) and (3). For practical purposes, Eqs. (2) and (3) are evaluated between $c_0 - 2.08$ and $c_0 + 2.08$ to ensure we encompass the entire beam pattern. Finally, the observed $K_{dp,obs}$ for a given elevation angle is found by one-half the range derivative of $\Phi_{DP,obs}$:

$$K_{dp,obs}(r, c_0) = \frac{1}{2}\frac{d\Phi_{dp;obs}(r;c_0)}{dr}: \quad (6)$$

As before, we exclude differential phase upon transmission as well as potential contributions to $\Phi_{DP,obs}$ from δ, which can exist in regions of non-Rayleigh scattering but which should be minimal in dry aggregated snow even at Ka band. Additionally, K_{dp} is calculated from Φ_{DP} locally; a multigate averaging window is not needed as for observations due to the absence of measurement noise.

We performed a control run simulation to demonstrate the basic behavior of the model using intrinsic profiles of Z and K_{dp} informed from Fig. 8. These profiles were not found by explicitly computing the electromagnetic scattering of hydrometeors with assumed characteristics (e.g., density, shape) but are simply defined to exist inherently. Similar to Case 2, the Z_{int} profile is prescribed to be 20 dBZ from the top of the model (assumed to be 6000 m) down to the top of the sublimation layer at 2000 m, and then rapidly decrease to 220 dBZ over the 500-m-deep layer. This decrease is modeled using a modified Gauss error function given by

$$Z_{int}(z) = Z_{int,min} + \frac{1}{2}(Z_{int,max} - Z_{int,min})[1 + \mathrm{erf}(z)], \quad (7)$$

where $Z_{int,min}$ and $Z_{int,max}$ are 220 and 20 dBZ, respectively, and erf(z) is given by

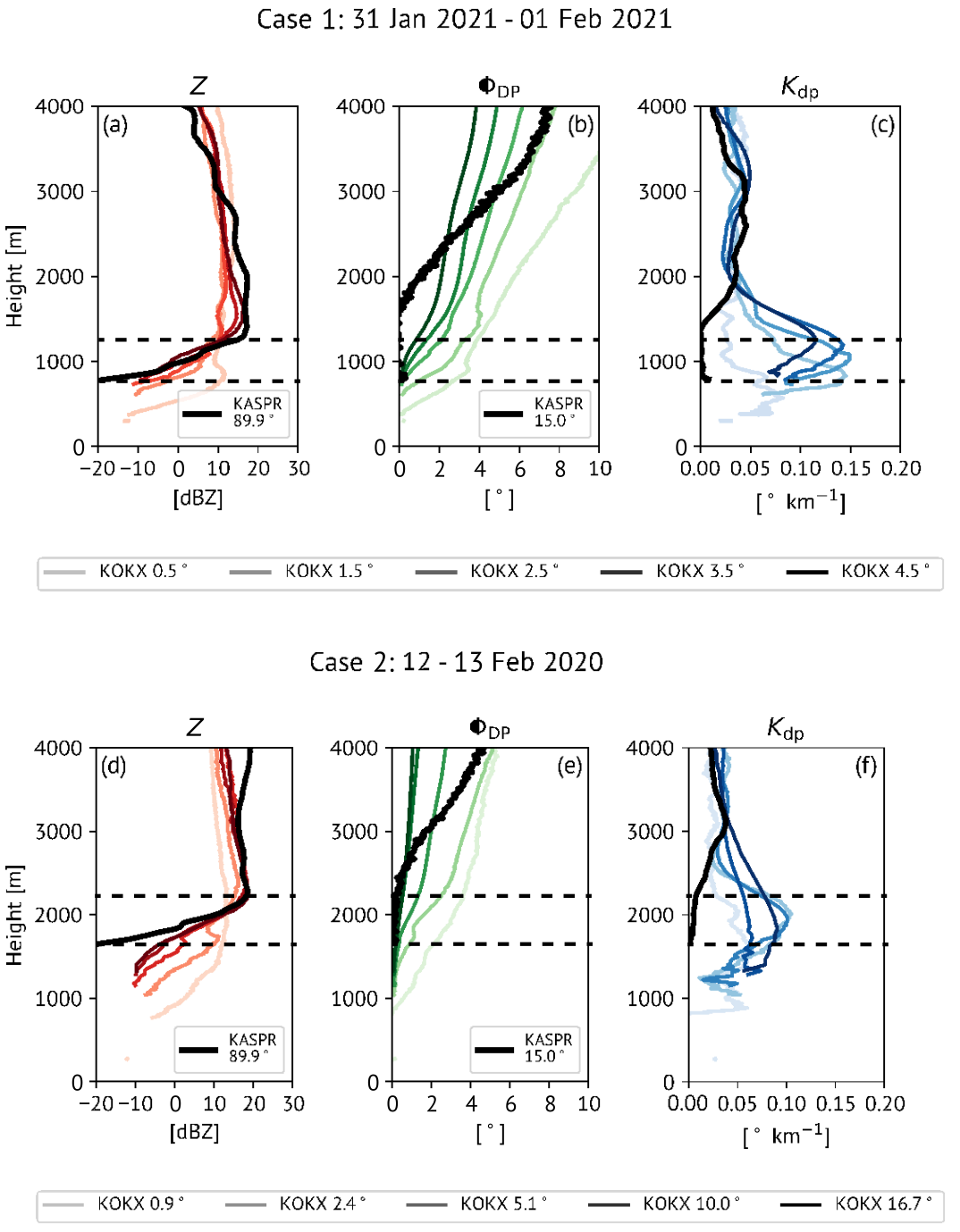

FIG. 8. Observed QVPs of (a),(d) Z (reds; dBZ), (b),(e) prefiltered F_{DP} (greens; 8), and (c),(f) K_{dp} (blues; 8 km^{21}) from KOKX for (a)–(c) Case 1 at all elevation angles and (d)–(f) Case 2 at select elevation angles. The KASPR profiles (black) in (a) and (d) are from the KASPR VPT scans while in (b), (c), (e), and (f) KASPR PPI data are used. The KOKX, KASPR VPT, and KASPR PPI scan times for Case 1 are 2257:46, 2305:32, and 2259:06 UTC, while for Case 2 they are 0050:00, 0045:47, and 0050:08 UTC, respectively. The sublimation layer is denoted by the dashed horizontal lines.

$$\mathrm{erf}(z) = \frac{2}{\sqrt{p}} \int_0^z e^{2x^2}\, dx \qquad (8)$$

to simulate a smooth transition into the sublimation layer. Similarly, $K_{dp,int}$ is assumed to be constant at 0.18 km^{21} down to the top of the sublimation layer and decrease to 0.08 km^{21} using an analogous modified Gauss error function. A VCP 32 (clear-air mode) scanning strategy is assumed.

The simulated profiles of Z_{obs} and $K_{dp,obs}$ for these control run intrinsic profiles are shown in Fig. 9. The impacts of beam

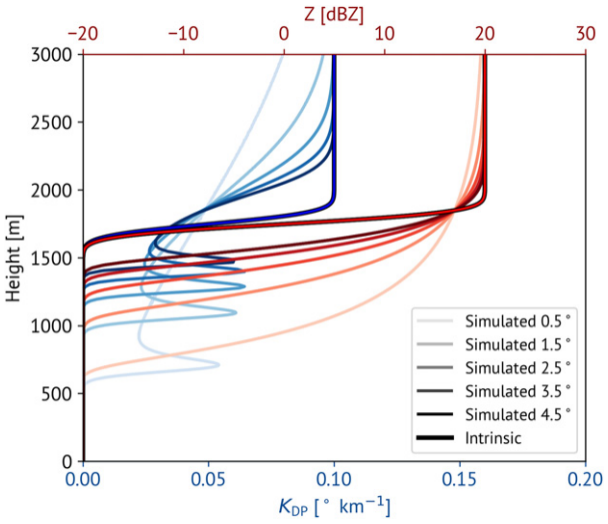

FIG. 9. Simulated vertical profiles of K_{dp} (8 km^{2} ^{1}; blue) and Z (dBZ; red) for a hypothetical NEXRAD VCP 32 (clear-air mode) scanning strategy using the NBF model of Ryzhkov and Zrnić (1998) described in text. Lines increase in darkness as the elevation angle increases.

broadening on the depiction of Z within the sublimation layer are immediately apparent, with the sharpness of the transition into the sublimation layer progressively more smeared at lower elevation angles and with Z_{obs} up to ′1000 m closer to the ground than Z_{int} for the 0.58 elevation angle. However, the effects are much more negligible by even the 4.58 elevation angle, which depicts a sharper transition into the sublimation layer and a fairly comparable height and slope of the Z gradient within it as Z_{int}. There is also a small negative bias of Z above the sublimation layer that is worse at lower elevation angles than higher ones. Both of these findings are in very good agreement with the observations in Fig. 8d for a sublimation layer around 2 km AGL, which shows Z observed up to 1000 m lower than the VPT KASPR data indicate, smeared transition zones, and negatively biased Z values above the sublimation layer that is worse for low elevation angles and diminishes for higher elevation angles.

In contrast, the simulated $K_{dp,obs}$ profiles exhibit pronounced impacts from NBF at all of the simulated elevation angles that resemble the observed K_{dp} QVPs in Figs. 8c and 8f. Compared to $K_{dp,int}$, a clear dipole bias exists, with a thin 200–300-m-deep layer of appreciably higher $K_{dp,obs}$ values up to 0.078 km^{21} beneath the sublimation layer (where $K_{dp,int}$ is 0.08 km^{21}) underneath a layer of gradually decreasing negative biases in $K_{dp,obs}$. This sort of NBF-induced dipole is reminiscent of the melting-layer simulations of Ryzhkov and Zrnić (1998), where they observed a positive K_{dp} bias below the melting level, negative bias within it, and another positive bias above it associated with the inverse Z gradient in the upper half of the radar brightband. The positive K_{dp} biases are quite peaked compared to the negative biases, which are more gradual and exist through a greater depth. In addition, unlike the impacts of beam broadening on Z, which suppressed the height of the Z_{obs} gradient to decidedly below that of Z_{int}, the $K_{dp,obs}$ profiles still feature an overall (weakened) gradient at the correct height, with the addition of the spike of erroneously high $K_{dp,obs}$ beneath the main sublimation-layer gradient. The height of the positively biased $K_{dp,obs}$ ascends and converges toward $K_{dp,int}$ with increasing elevation angle while the overall depth of the bias dipole decreases slightly. However, even for the 4.58 elevation scan with reduced beam broadening impacts on Z, the induced positive $K_{dp,obs}$ bias remains comparable to those from lower elevation angles. The simulated positive $K_{dp,obs}$ peaks are narrower than those observed, although this discrepancy is expected due to both K_{dp} processing within a multigate window and additional smearing due to azimuthal averaging of heterogeneities. With independent remote sensing evidence suggesting that the observed sublimation-layer K_{dp} enhancements at KOKX are not due to SIP (see section 2b) and the marked agreement with the QVP observations in Fig. 8, these simulation results strongly suggest that these enhancements are an artifact due to NBF.

We explored the impact of the intrinsic precipitation characteristics by systematically modifying the Z_{int} and $K_{dp,int}$ profiles from the control run. In Fig. 10a, the sublimation layer was extended to a depth of 1000 m instead of the 500-m default depth. The sublimation layer was also shifted upward by 250 m to keep the center of the sublimation layer at the same height as the control run. The resultant $K_{dp,obs}$ biases show a stronger sensitivity to elevation angle than the control run. The profiles from lower elevation angles look very similar to the control run due to saturation of the beamwidth with respect to the sublimation layer. For example, at the 0.58 elevation angle, once the lower edge of the 1.08-wide beam reaches 1500 m (i.e., the bottom of the sublimation layer), the top of the beam has already reached nearly 4300 m, putting the entire sublimation layer within the beam in both the control and this modified profile. In contrast, at higher elevation angles, the induced positive $K_{dp,obs}$ bias is noticeably smaller than in the control run. The corresponding beamwidth at the 4.58 elevation angle is just 368 m. This finding is intuitive, as a weaker Z gradient results in lesser diversity within the radar beam of a given size. However, this finding also hints at the nature of how these NBF effects may obfuscate any (likely small) true enhancements of K_{dp} due to SIP, as drier air that results in stronger sublimation, sharper Z gradients, and more potential for snow to make it into sufficiently dry air to sublimate and undergo SIP (e.g., relative humidity with respect to ice # 70%; Oraltay and Hallett 1989) will also contribute to stronger artificial K_{dp} enhancements.

The impact of the sublimation-layer height is examined in Fig. 10b, where the sublimation layer has been shifted down to 1 km AGL. In this case, the biases at all but the lowest elevation angles are minimal compared to when the sublimation layer was higher. These results again clearly demonstrate the relation between the degree of beam broadening and the severity of the NBF impacts. While the corresponding 0.58-elevation-angle beamwidth is 1600 m by the time the bottom of the beam has reached the sublimation layer (at a range of ′92 km), and we see similar $K_{dp,obs}$ enhancements as the control run, the

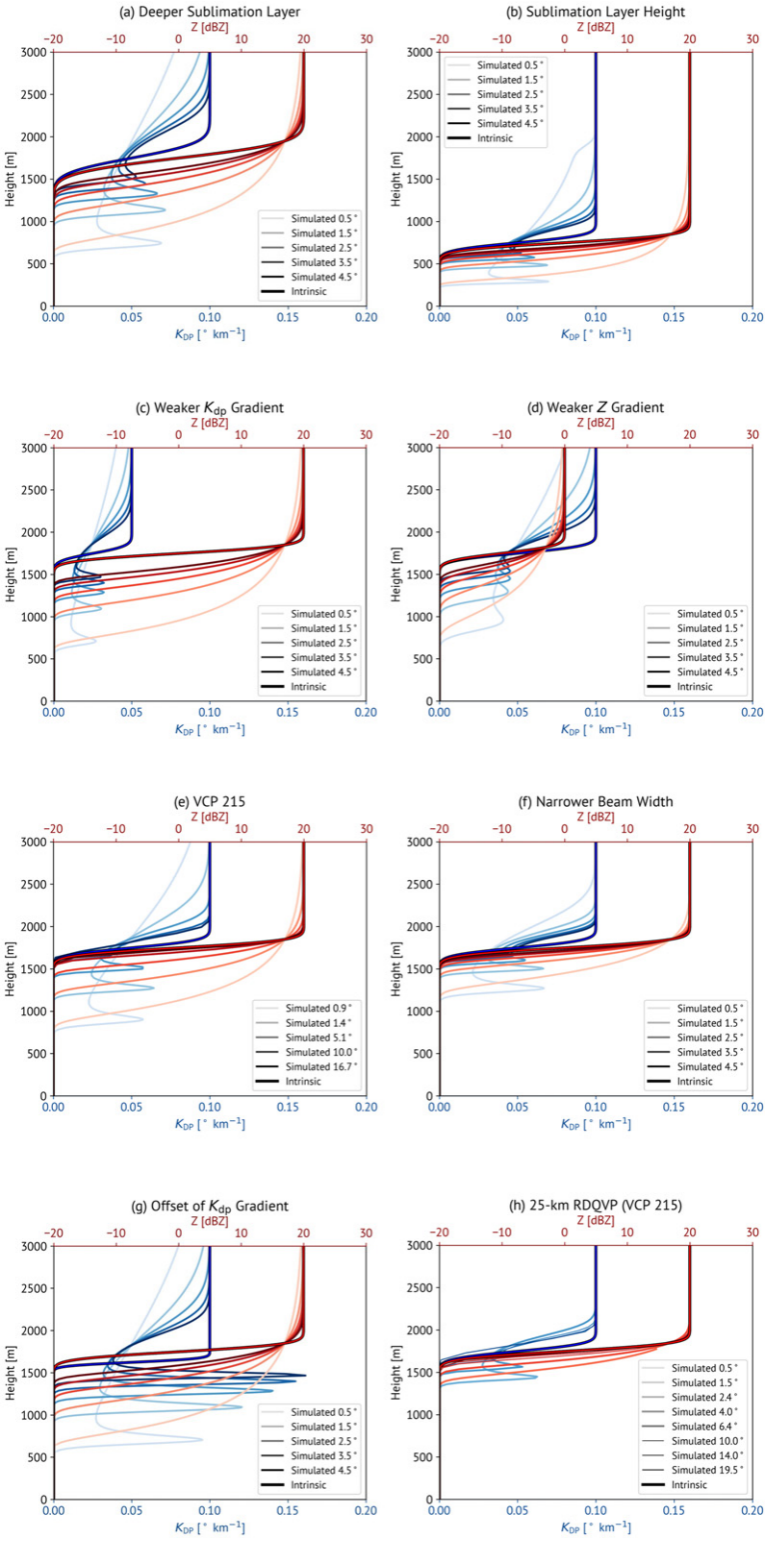

FIG. 10. As in Fig. 9, but for (a) a deeper sublimation-layer depth, (b) a lower sublimation-layer height, (c) a weaker F_{DP} gradient, (d) a weaker Z gradient, (e) VCP 215, (f) a narrower beamwidth of 0.328, (g) an offset of the K_{dp} gradient, and (h) a 25-km RDQVP using the VCP 215 scanning strategy.

4.58-elevation-angle beamwidth is just 128 m (at a range of ′7 km), minimizing the degree of variability within the beam. This likely explains, at least in part, the consistent appearance of the enhanced K_{dp} in the sublimation layer at altitudes higher than ′1–2 km AGL in both Carlin et al. (2021) and Figs. 2 and 5. Finally, the magnitudes of the $K_{dp,int}$ and Z_{int} above the sublimation layer also affect the resultant biases due to NBF. The $K_{dp,int}$ was halved in Fig. 10c, with the attendant $K_{dp,obs}$ biases below the sublimation layer maintaining their shape but with their magnitudes proportionately smaller. A halving of Z_{int} above the sublimation layer (and subsequently the magnitude of the gradient within it) also diminishes the impacts of NBF, but primarily minimizes the peak magnitude and prominence of the positive $K_{dp,obs}$ biases while maintaining the overall higher values compared to $K_{dp,int}$ below the sublimation layer. Taken together, these results speak to the overwhelming impact of the radar's elevation angles on determining the impacts of NBF, as the observed biases are worse in Fig. 8c despite Fig. 8f having a sharper Z gradient and higher sublimation layer, both of which otherwise worsen NBF effects.

We also performed sensitivity tests regarding radar characteristics and scanning and processing strategies. Figure 10e shows the default intrinsic profiles but scanned with VCP 215 (precipitation mode). For the sake of clarity only five select elevation angles are shown. Unsurprisingly, the amount of broadening of the sublimation layer in Z_{obs} and NBF impacts on $K_{dp,obs}$ are strongly diminished at higher elevation angles, as the beams are still relatively narrow when intersecting the intrinsic profiles and do so at a more oblique angle, diminishing the variability of the intrinsic variables within the beam. This, in part, likely explains why K_{dp} enhancements in the sublimation layer were never apparent in the KASPR data, as the PPI scanning angle was fixed at 15.08; the comparable 16.78 elevation angle profile from KOKX shows only a slight negative bias in the upper portion of the sublimation layer with no positive $K_{dp,obs}$ peak beneath it. However, an even more dramatic effect is seen for a modified beamwidth. Figure 10f shows the default profile but for KASPR's beamwidth of 0.328. While there is still a pronounced $K_{dp,obs}$ bias at the 0.58 elevation angle, this rapidly diminishes and becomes quite minor for elevation angles greater than 2.58 as the beamwidth is narrower by approximately a factor of 1.0/0.32. Rather than the chosen K_{dp} processing routine or any difference in precipitation characteristics between the two sites, it is very likely that the combination of KASPR's narrow beamwidth and its fixed elevation angle at 15.08 eliminated any impacts of beam broadening and NBF on the observed Φ_{DP} and explains the consistent lack of any K_{dp} enhancement in the sublimation layer from KASPR despite its shorter wavelength that should, all else being equal, make NBF effects much worse.

While the simulations presented in Figs. 9 and 10 bear an overall close resemblance to the observed Z and K_{dp} profiles (e.g., Fig. 8), the magnitude of the observed K_{dp} enhancements is bigger than the simulated ones (roughly 0.108–0.158 km^{21} versus 0.078 km^{21}, respectively). An additional sensitivity test where the $K_{dp,int}$ gradient is located in the lower half of the sublimation layer was performed and is shown in Fig. 10g. The effect of this change on the resultant positive $K_{dp,obs}$ biases is striking and dwarfs the impact of all other sensitivity tests thus far, with the peak magnitudes more than doubling to over 0.158 km^{21}. This can be understood using the vectors in Fig. A1 in the appendix, as larger $K_{dp,int}$ coincident with a Z_{int} gradient causes more dramatic rotation of the vectors and subsequent NBF effects. While it is reasonable to expect the majority of small particles that contribute to the bulk of K_{dp} to sublimate quickly in the upper portions of the sublimation layer, remaining uncertainty associated with defining a representative $K_{dp,int}$ profile and the observed variability on a radial-by-radial basis that contributes to the azimuthally averaged profile may explain the remaining gap between the magnitudes of the simulations and observed profiles.

Another apparent curiosity arises that concerns the clarity of the K_{dp} enhancement when averaging the various elevation angles together during RDQVP processing. Due to the dipole nature of the K_{dp} bias at each elevation angle, it seems intuitive that there would be appreciable destructive interference between the elevation angles that would minimize the overall extent of the NBF impacts. Ryzhkov and Zrnić (1998) observed a similar negation of biases for isolated rain cells, where little overall bias was observed in the total areal rainfall. However, Fig. 10h shows the default profile when limited to what would be included in the averaging for an RDQVP with a 25-km cutoff radius (applied to VCP 215 elevation angles). Because the lower elevation angles do not reach sufficient heights to be affected by NBF before exiting the 25-km-range threshold, their negative bias region coinciding with the positive biases from higher elevation angles (e.g., Fig. 9) are excluded from the averaged profile. In addition, the height of the peak $K_{dp,obs}$ enhancement gradually converges with increasing elevation angle. Therefore, such a cutoff allows for the enhancement regions from intermediate elevation angles to constructively reinforce each other and produce a clear signal.

This is further examined in Fig. 11, which shows the averaged RDQVP for the enhanced K_{dp} bias case (i.e., Fig. 10g) as a function of RDQVP cutoff range. The artificial K_{dp} enhancement peaks at intermediate but fairly short averaging radii [e.g., roughly 20–25 km for VCP 32 (clear-air mode) and at 13 km for VCP 215 (precipitation mode)]. At very short averaging radii, the lower elevation angles that experience the most severe NBF effects get cut off before those effects can be incorporated into the average profile, and at larger averaging radii more of the lower elevation angles' negative dipole regions are incorporated into the averaging that reduces the magnitude of the overall bias. In contrast to this, the effects of beam broadening on Z are maximized for the largest averaging radii for both VCPs, as more influence from the most-smeared lowest elevation angles are able to be incorporated into the average profile at the sublimation-layer height. As stated before, this example should be considered conservative, as deeper and more prominent enhancements due to azimuthal heterogeneity and the use of multigate averaging windows would result in more constructive interference and clearer K_{dp} biases in real RDQVPs.

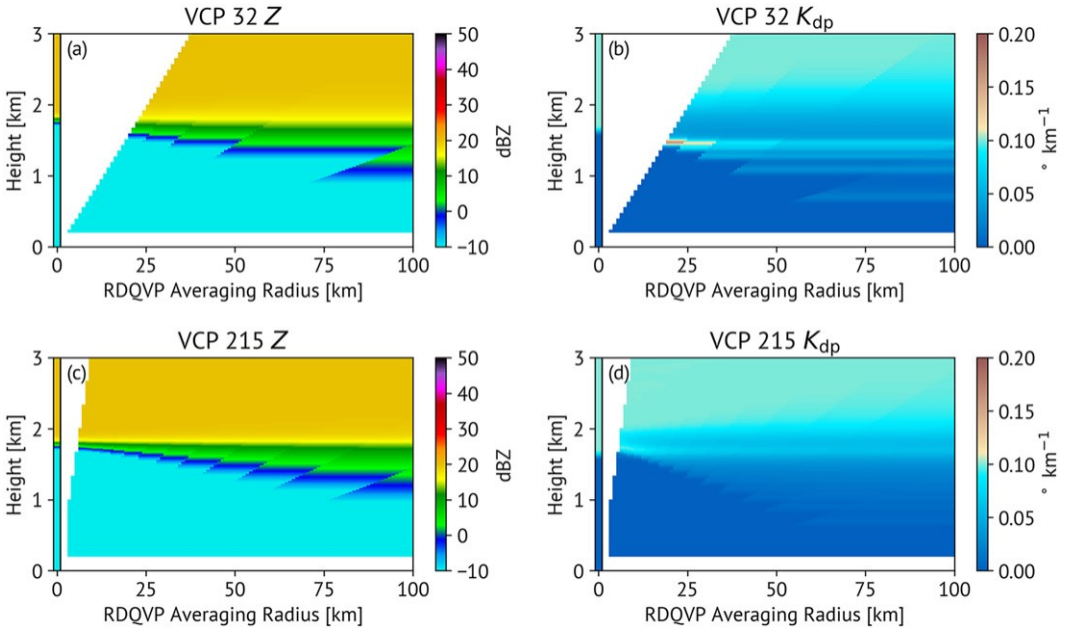

FIG. 11. Simulated RDQVPs of (a),(c) Z and (b),(d) K_{dp} as a function of RDQVP averaging radius for (a),(b) clear-air mode (VCP 32) and (c),(d) precipitation mode (VCP 215) taking into account beam-broadening and NBF effects. The profiles at a range of 0 km are the intrinsic profiles.

4. Discussion and conclusions

In this study, we explored two cases of sublimating snow exhibiting a layer of enhanced K_{dp}. These enhancements have previously been hypothesized to result from SIP (Carlin et al. 2021) and thus were examined in more detail using a collocated S-band WSR-88D radar and a Ka-band research radar. The signature has been frequently observed at S band but not at Ka band, where any K_{dp} enhancement within the Rayleigh scattering regime should be much more apparent. The absence of a distinct population of particles produced through sublimational SIP was confirmed via vertically pointing Doppler spectra and spectral LDR observations as well as through PPIs and QVPs of other polarimetric variables. Using the beam-broadening model of Ryzhkov and Zrnić (1998), we showed that the observed K_{dp} enhancements likely result from the effects of NBF in the presence of a very strong Z gradient within the sublimating snow. This NBF results in a K_{dp} bias dipole in the vertical; constructive interference of these profiles from different elevation angles was shown to be possible due to range thresholds used in RDQVP processing. Sensitivity tests revealed a response of this NBF artifact to the strength of the Z gradient (which is related to the degree of subsaturation in the dry layer), the height at which it occurs, the radar's elevation angles, the aforementioned range cutoff during RDQVP processing, and the radar beamwidth. It is believed that the relatively high (158) elevation angle together with the narrow beamwidth of the Ka-band radar nearly eliminated the impact of NBF compared to the S-band radar, despite it having an intrinsic K_{dp} over 12 times larger and NBF effects being more severe at shorter wavelengths.

This presumed misinterpretation of polarimetric evidence of SIP due to sublimation put forth in Carlin et al. (2021) may serve as a cautionary tale regarding the importance of considering the effects of beam broadening when interpreting polarimetric signatures, especially when presented in an azimuthally averaged time–height format where such effects may be obfuscated. Case studies of SIP due to sublimation are particularly ripe for misinterpretation because the factors believed to contribute to and be evidence of SIP}sufficiently large Z entering the sublimation layer indicative of large aggregates and sufficiently dry air to rapidly sublimate the snow within a confined layer}are the same factors that directly contribute to stronger K_{dp} enhancements due to the impacts of NBF on F_{DP}. Paradoxically, any genuine K_{dp} enhancements within the sublimation layer (e.g., caused by SIP due to sublimation or turbulence-enhanced collisional breakup) will worsen these NBF impacts, further obscuring the enhancement. Similarly, some of the observation-based assumptions made in the beam broadening model}namely, the uniformity of Z_{dr} and $|r_{hv}|$ within the sublimation layer}may not strictly hold, as the variability in the supporting observations could be muted due to beam broadening as well. The bands of enhanced K_{dp} remain perfectly coincident with the Z gradient as it descends and occur low enough into the sublimation layer so as to be collocated with very low RH_i, a necessary condition for prolific SIP (e.g., Oraltay and Hallett 1989). The cohesion of this band and its maximum values, along with its appearance and demise now believed to be due to the geometry of the VCP and the RDQVP processing, were consistent with the interpretation K_{dp} enhancements believed to be due to other SIP mechanisms.

Even as K_{dp} is increasingly shown to be a crucial element of polarimetric microphysical retrievals in snow (Ryzhkov et al. 1998; Bukovčić et al. 2018, 2020; Ryzhkov and Zrnić 2019; Hu and Ryzhkov 2022; Dunnavan et al. 2022; Blanke et al. 2022), the development of methods for accurately calculating K_{dp} remains an active area of research, with no single best agreed-upon approach for all circumstances (Reimel and Kumjian 2021). Herein, we also explored calculating K_{dp} using the method employed operationally by the U.S. National Weather Service (Ryzhkov et al. 2005); the overall qualitative conclusions remained the same, but quantitative differences in the magnitude of the K_{dp} enhancements and agreement with the KASPR observations were observed. Separate from areas of NBF, regions of nonnegligible d, ground clutter, nonmeteorological scatterers, and measurement noise all contribute to the need for robust filtering of F_{DP} prior to computing K_{dp}. Filtering techniques proposed to calculate K_{dp} from F_{DP} that rely on constraints of F_{DP} increasing monotonically along the radial, such as linear programming (Giangrande et al. 2013), have cited areas of NBF as regions where such approaches should not be used. However, examples of such instances have historically been regions of sharp azimuthal Z gradients (such as occurs in squall lines oriented parallel to the radar beam) or in sharp vertical Z gradients within stratiform precipitation melting layers (Giangrande et al. 2013). While the values of Z within snow sublimation layers are typically low with noisy F_{DP} that make the accurate computation of K_{dp} inherently difficult, the increasingly widespread adoption of radar processing techniques that azimuthally or spatially average radar data to obtain estimates of the polarimetric variables with reduced noise has revealed other scenarios of prohibitive impacts of vertical NBF in snow, which have not historically received attention. Because the scale of the impacts of NBF are quite small compared to that seen in intense convection, we did not observe the characteristic drop of r_{hv} down-radial from the NBF (e.g., Ryzhkov 2007). Despite this, we have demonstrated that the impact on F_{DP} is significant enough to impact the calculation of the small values of K_{dp} in snow that become robust enough to use with azimuthal averaging.

Despite the new interpretation of the enhanced K_{dp} regions reported in Carlin et al. (2021), we do not mean to imply that SIP due to sublimation never occurs in these layers of pronounced snow sublimation but rather that our ability to observe it using typical operational radars and scanning strategies may be limited due to the contamination by NBF. There remains robust, if limited, laboratory evidence of SIP due to sublimation of both dendritic snow crystals and rimed graupel particles, and the results herein do not necessarily support either side of the debate regarding the ultimate importance of sublimational SIP. Future work should explore applying the beam broadening model presented here to explicit simulations of SIP due to sublimation [e.g., using the scheme of Deshmukh et al. (2022) coupled to a polarimetric radar forward operator] that may alleviate some of the assumptions made in deriving Eq. (2). Additionally, more in situ data collected in regions of strong sublimation similar to the cases studied here will help address the remaining ambiguities regarding SIP due to sublimation.

Acknowledgments. Funding for authors Carlin, Dunnavan, and Ryzhkov was provided by NOAA/Office of Oceanic and Atmospheric Research under NOAA–University of Oklahoma Cooperative Agreement NA21OAR4320204, U.S. Department of Commerce, and for authors Dunnavan and Ryzhkov by National Science Foundation Grant AGS-1841246. Author Oue acknowledges support from National Science Foundation Grants AGS-01841215 and AGS-1904809 and from the National Aeronautics and Space Administration Grant 80NSSC19K0394. The authors thank Valery Melnikov for his constructive comments that improved this manuscript as well as Haoran Li and a second anonymous reviewer for their helpful and thorough reviews.

Data availability statement. KASPR data are available from https://doi.org/10.5067/IMPACTS/RADAR/DATA101, whereas WSR-88D data are made available on many different websites such as https://registry.opendata.aws/noaa-nexrad/. The Python-based beam-broadening model code can be made available upon request.

APPENDIX

Physical Explanation of Nonuniform Beam Filling Effects

Herein, we provide a physical explanation of the NBF effect. We define a precipitation slab located at height H with stepwise vertical profiles of Z and K_{dp} (i.e., Z and K_{dp} are constant above height H and zero below H; Fig. A1a), with no explicit sublimation-layer gradients for simplicity. Consider three narrow subbeams within the antenna pattern that approach and intersect the precipitation layer at height H at different ranges and, correspondingly, at different times. One of them corresponds to the beam center at elevation angle c_0 and the others near the top and the bottom of the beam at elevation angles c_0 1 Dc and c_0 2 Dc, respectively. The total F_{DP} is a function of the contributions from each of these subbeams. In this simplified example and as defined in Eq. (2), the total F_{DP} is equal to the phase of the sum of the three complex vectors (or phasors) representing the central subbeam (a_c) and the two off-center subbeams at the top (a_t) and bottom (a_b) of the beam. The expressions for these phasors can be written as

$$a_c = A_c e^{jF_{DP}(r)} = A_c e^{2jK_{dp}(r-r_c)} \tag{A1}$$

and

$$a_{t,b} = A_{t,b} e^{jF_{DP}(r)} = A_{t,b} e^{2jK_{dp}(r-r_{t,b})}, \tag{A2}$$

where the phasor amplitudes are defined as

$$A_c = ZI(c_0, c_0), \tag{A3}$$

when r . r_c and

$$A_{t,b} = ZI(c_0 \pm Dc, c_0), \tag{A4}$$

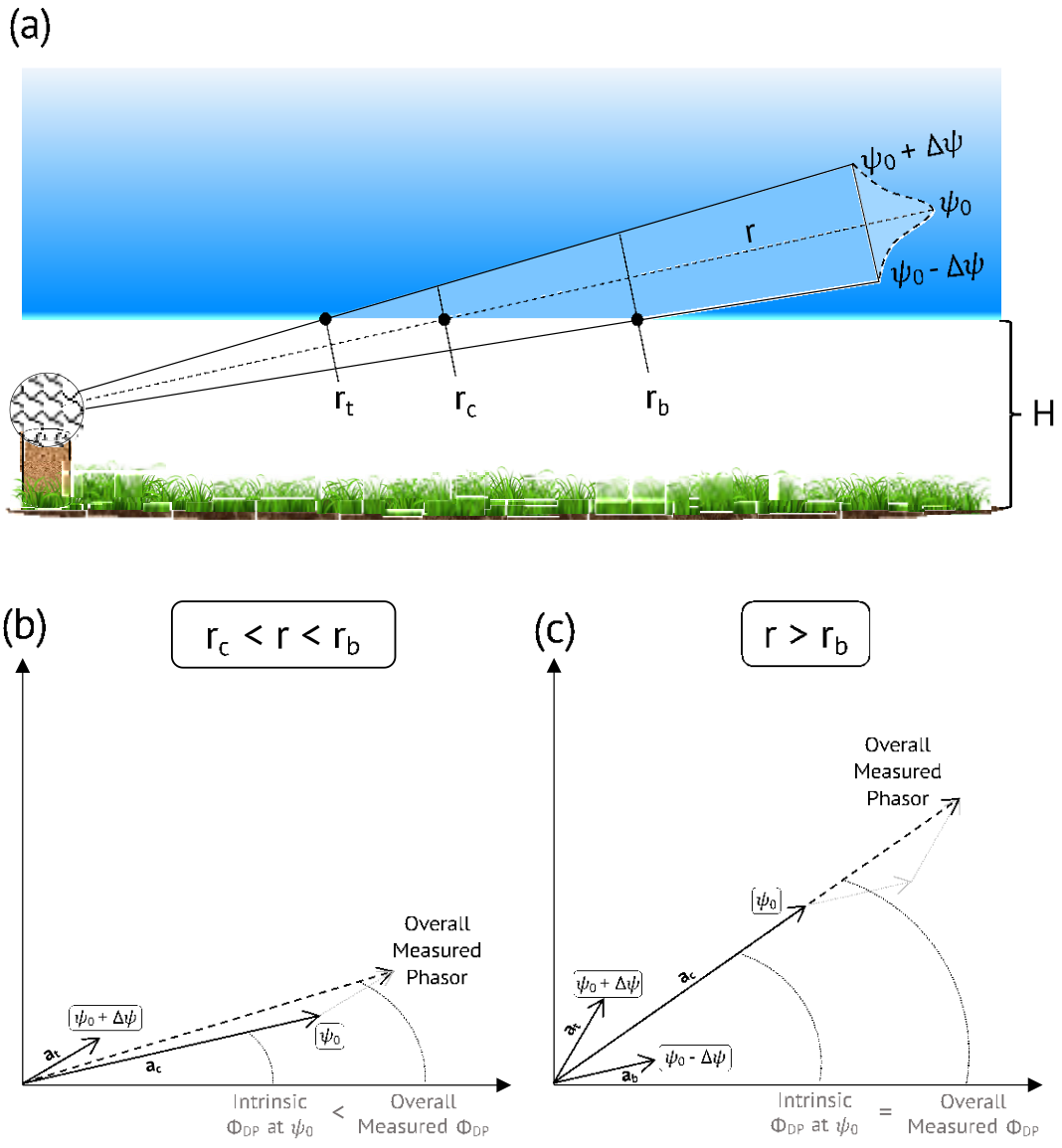

FIG. A1. Graphical representation of the effects of nonuniform beam filling. (a) Cartoon representing the radar beam intersecting a slab precipitation layer that begins at height H. The shading represents uniform Z and K_{dp} fields while r_t, r_c, and r_b represent the ranges at which the top, center, and bottom of the beam intersect the precipitation layer, respectively. The beam center is at elevation angle c_0, with off-center locations within the beam pattern located at c_0 6 Dc, and phasors a_t, a_c, and a_b as described in text. (b),(c) Phasor diagrams showing representative vectors associated with the denoted locations within the beam pattern at (b) intermediate ranges before the entire beam has entered the precipitation layer and (c) ranges once the entire beam is within the precipitation layer compared to the overall measured vector integrated across the beamwidth.

when r . $r_{t,b}$. In Eqs. (A3) and (A4), I is the Gaussian beam pattern weighting function given by Eq. (4). Because Z is uniform above H but the beam power is maximized at c_0, A_c . $A_{t,b}$ once the respective range thresholds are met.

It can be inferred from Eqs. (A1) and (A2) that, due to the assumption of a constant K_{dp} in the precipitation layer, the phase difference between the three phasors is constant at all ranges r. This means that the phasors rotate synchronously with increasing r. However, at distances r_c , r , r_b, the phasor a_t adds to the phasor a_c in such a way that the total differential phase becomes larger than the one associated with the phase of a_c, which alone represents the case of an infinitesimally narrow antenna beam with no NBF impacts (Fig. A1b). At longer distances (i.e., r . r_b) where all three subbeams are within the precipitation layer, all three phasors are summed up and the direction of the overall resultant phasor coincides with the direction of a_c, eliminating the impact of NBF (Fig. A1c). This simple scheme explains

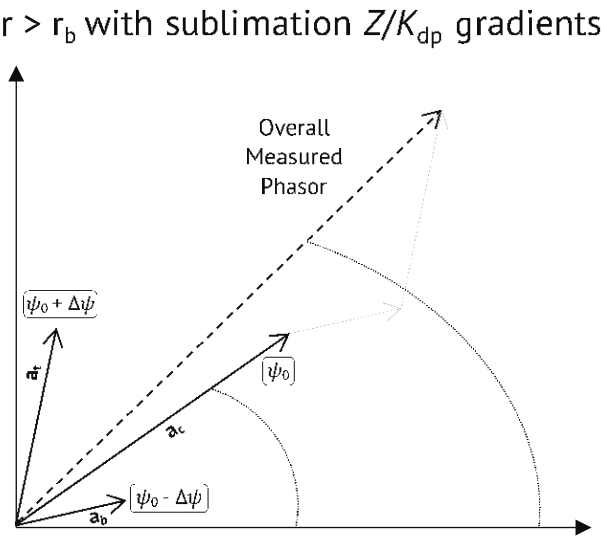

FIG. A2. As in Fig. A1c, but in the presence of Z and K_{dp} increasing upward within the sublimation layer.

the measured bump in the radial profile of the F_{DP} from Eq. (2) (i.e., at ranges prior to the entire beam being within the homogeneous precipitation layer), which causes a "dipole" bias K_{dp} signature compared to the intrinsic K_{dp} profile.

It is clear that the NBF effect is dependent on the antenna beamwidth and on the value of the incidence angle of the electromagnetic wave entering the precipitation slab. For the extreme case of normal incidence (i.e., a zenith-pointing angle), the contributions from the vectors a_b and a_t are equal at all distances from the radar and there is no NBF impact on the radial profile of F_{DP}. The magnitude of the NBF effect depends on the degree of asymmetry between the contributions of the off-center subbeams a_t and a_b to the vector sum. Such an asymmetry becomes larger as the range differences r_c 2 r_t and r_b 2 r_c increase, which happens for broader beams and lower incidence angles. It also becomes larger with vertical gradients of Z and K_{dp} as seen in sublimation layers. K_{dp} increasing upward increases the angle difference between a_t and a_c when r . r_c and between a_c and a_b when r . r_b (Fig. A2). Similarly, Z increasing upward makes the magnitude of a_t larger relative to a_c and causes further rotation of the overall measured phasor, as well as increasing the asymmetry between the two off-center subbeams. As such, vertical gradients of the radar variables within sublimation layers further magnifies the effects of NBF to observable levels, even in snow.

REFERENCES

Bacon, N. J., B. D. Swanson, M. B. Baker, and E. J. Davis, 1998: Breakup of levitated frost particles. J. Geophys. Res., 103, 13 763–13 775, https://doi.org/10.1029/98JD01162.

Blanke, A., A. Heymsfield, M. Moser, and S. Trömel, 2022: Evaluation of state-of-the-art polarimetric ice microphysical retrievals exploiting ground based radar and airborne measurements. EGU General Assembly 2022, Vienna, Austria, EGU, EGU22-7623.

Bodas-Salcedo, A., J. P. Mulcahy, T. Andrews, K. D. Williams, M. A. Ringer, P. R. Field, and G. S. Elsaesser, 2019: Strong dependence of atmospheric feedbacks on mixed-phase microphysics and aerosol-cloud interactions in HadGEM3. J. Adv. Model. Earth Syst., 11, 1735–1758, https://doi.org/10.1029/2019MS001688.

Buck, A. L., 1981: New equations for computing vapor pressure and enhancement factor. J. Appl. Meteor. Climatol., 20, 1527–1532, https://doi.org/10.1175/1520-0450(1981)020,1527:NEFCVP.2.0.CO;2.

} } , 1996: Model CR-1A hygrometer with autofill operating manual. Buck Research Instruments Operating Manual, 26 pp., https://www.hygrometers.com/wp-content/uploads/CR-1A-users-manual-2009-12.pdf.

Bukovčić, P., A. Ryzhkov, D. Zrnić, and G. Zhang, 2018: Polarimetric radar relations for quantification of snow based on disdrometer data. J. Appl. Meteor. Climatol., 57, 103–120, https://doi.org/10.1175/JAMC-D-17-0090.1.

} } , } } , and } } , 2020: Polarimetric relations for snow estimation}Radar verification. J. Appl. Meteor. Climatol., 59, 991–1009, https://doi.org/10.1175/JAMC-D-19-0140.1.

Carlin, J. T., H. D. Reeves, and A. V. Ryzhkov, 2021: Polarimetric observations and simulations of sublimating snow: Implications for nowcasting. J. Appl. Meteor. Climatol., 60, 1035–1054, https://doi.org/10.1175/JAMC-D-21-0038.1.

Deshmukh, A., V. T. J. Phillips, A. Bransemer, S. Patade, and D. Waman, 2022: New empirical formulation for the sublimational breakup of graupel and dendritic snow. J. Atmos. Sci., 79, 317–336, https://doi.org/10.1175/JAS-D-20-0275.1.

Dong, Y., R. G. Oraltay, and J. Hallett, 1994: Ice particle generation during evaporation. Atmos. Res., 32, 45–53, https://doi.org/10.1016/0169-8095(94)90050-7.

Doviak, R. J., and D. S. Zrnic, 1993: Doppler Radar and Weather Observations. 2nd ed. Academic Press, 562 pp.

Dunnavan, E. L., and Coauthors, 2022: Radar retrieval evaluation and investigation of dendritic growth layer polarimetric signatures in a winter storm. J. Appl. Meteor. Climatol., 61, 1685–1711, https://doi.org/10.1175/JAMC-D-21-0220.1.

Field, P. R., and Coauthors, 2017: Secondary ice production: Current state of the science and recommendations for the future. Ice Formation and Evolution in Clouds and Precipitation: Measurement and Modeling Challenges, Meteor. Monogr., No. 58, Amer. Meteor. Soc., https://doi.org/10.1175/AMSMONOGRAPHS-D-16-0014.1.

Giangrande, S. E., R. McGraw, and L. Lei, 2013: An application of linear programming to polarimetric radar differential phase processing. J. Atmos. Oceanic Technol., 30, 1716–1729, https://doi.org/10.1175/JTECH-D-12-00147.1.

Grazioli, J., G. Lloyd, L. Panziera, C. R. Hoyle, P. J. Connolly, J. Henneberger, and A. A. Berne, 2015: Polarimetric radar and in situ observations of riming and snowfall microphysics during CLACE 2014. Atmos. Chem. Phys., 15, 13 787–13 802, https://doi.org/10.5194/acp-15-13787-2015.

Griffin, E. M., T. J. Schuur, and A. V. Ryzhkov, 2018: A polarimetric analysis of ice microphysical processes in snow, using quasi-vertical profiles. J. Appl. Meteor. Climatol., 57, 31–50, https://doi.org/10.1175/JAMC-D-17-0033.1.

Hallett, J., and S. C. Mossop, 1974: Production of secondary ice particles during the riming process. Nature, 249, 26–28, https://doi.org/10.1038/249026a0.

Helmus, J. J., and S. M. Collis, 2016: The Python ARM Radar Toolkit (Py-ART), a library for working with weather radar data in the python programming language. J. Open Res. Software, 4, e25, https://doi.org/10.5334/jors.119.

Hu, J., and A. Ryzhkov, 2022: Climatology of the vertical profiles of polarimetric radar variables and retrieved microphysical parameters in continental/tropical MCSs and landfalling hurricanes. J. Geophys. Res. Atmos., 127, e2021JD035498, https://doi.org/10.1029/2021JD035498.

Hubbert, J. C., and V. N. Bringi, 1995: An iterative filtering technique for the analysis of copolar differential phase and dual-frequency radar measurements. J. Atmos. Oceanic Technol., 12, 643–648, https://doi.org/10.1175/1520-0426(1995)012,0643:AIFTFT.2.0.CO;2.

Kollias, P., and M. Oue, 2020: SBU Ka-band Scanning Polarimetric Radar (KASPR) IMPACTS, version 1. NASA Global Hydrology Resource Center DAAC, accessed 24 Feb 2022, https://doi.org/10.5067/IMPACTS/RADAR/DATA101.

Korolev, A., and T. Leisner, 2020: Review of experimental studies of secondary ice production. Atmos. Chem. Phys., 20, 11 767–11 797, https://doi.org/10.5194/acp-20-11767-2020.

Kudo, A., 2013: The generation of turbulence below midlevel cloud bases: The effect of cooling due to sublimation of snow. J. Appl. Meteor. Climatol., 52, 819–833, https://doi.org/10.1175/JAMC-D-12-0232.1.

Kumjian, M. R., 2013a: Principles and applications of dual-polarization weather radar. Part I: Description of the polarimetric radar variables. J. Oper. Meteor., 1, 226–242, https://doi.org/10.15191/nwajom.2013.0119.

} } , 2013b: Principles and applications of dual-polarization weather radar. Part II: Warm- and cold-season applications. J. Oper. Meteor., 1, 243–264, https://doi.org/10.15191/nwajom.2013.0120.

} } , and K. A. Lombardo, 2017: Insights into the evolving microphysical and kinematic structure of northeastern U.S. winter storms from dual-polarization Doppler radar. Mon. Wea. Rev., 145, 1033–1061, https://doi.org/10.1175/MWR-D-15-0451.1.

} } , S. Mishra, S. E. Giangrande, T. Toto, A. V. Ryzhkov, and A. Bansemer, 2016: Polarimetric radar and aircraft observa-tions of saggy bright bands during MC3E. J. Geophys. Res. Atmos., 121, 3584–3607, https://doi.org/10.1002/2015JD024446. } } , D. M. Tobin, M. Oue, and P. Kollias, 2020: Microphysical insights into ice pellet formation revealed by fully polarimetric Ka-band Doppler radar. J. Appl. Meteor. Climatol., 59, 1557–1580, https://doi.org/10.1175/JAMC-D-20-0054.1.

Li, H., and D. Moisseev, 2020: Two layers of melting ice particles within a single radar bright band: Interpretation and implications. Geophys. Res. Lett., 47, e2020GL087499, https://doi.org/10.1029/2020GL087499.

} } , O. Mohler, T. Petaja, and D. Moisseev, 2021: Two-year statistics of columnar-ice production in stratiform clouds over Hyytiala, Finland: Environmental conditions and the relevance to secondary ice production. Atmos. Chem. Phys., 21, 14 671–14 686, https://doi.org/10.5194/acp-21-14671-2021.

May, R. M., S. C. Arms, P. Marsh, E. Bruning, J. R. Leeman, K. Goebbert, J. E. Thielen, and Z. S. Bruick, 2022: MetPy: A Python package for meteorological data. UCAR Unidata, https://doi.org/10.5065/D6WW7G29.

McMurdie, L. A., and Coauthors, 2022: Chasing snowstorms: The Investigation of Microphysics and Precipitation for Atlantic Coast-Threatening Snowstorms (IMPACTS) campaign. Bull. Amer. Meteor. Soc., 103, E1243–E1269, https://doi.org/10.1175/BAMS-D-20-0246.1.

Morrison, H., and Coauthors, 2020: Confronting the challenge of modeling cloud and precipitation microphysics. J. Adv. Model. Earth Syst., 12, e2019MS001689, https://doi.org/10.1029/2019MS001689.

Oraltay, R. G., and J. Hallett, 1989: Evaporation and melting of ice crystals: A laboratory study. Atmos. Res., 24, 169–189, https://doi.org/10.1016/0169-8095(89)90044-6.

Oue, M., M. R. Kumjian, Y. Lu, J. Verlinde, K. Aydin, and E. E. Clothiaux, 2015: Linear depolarization ratios of columnar ice crystals in a deep precipitating system over the Arctic observed by zenith-pointing Ka-band Doppler radar. J. Appl. Meteor. Climatol., 54, 1060–1068, https://doi.org/10.1175/JAMC-D-15-0012.1.

} } , P. Kollias, A. Ryzhkov, and E. P. Luke, 2018: Toward exploring the synergy between cloud radar polarimetry and Doppler spectral analysis in deep cold precipitation systems in the Arctic. J. Geophys. Res. Atmos., 123, 2797–2815, https://doi.org/10.1002/2017JD027717.

Patade, S., and Coauthors, 2022: The influence of multiple groups of biological ice nucleating particles on microphysical properties of mixed-phase clouds observed during MC3E. Atmos. Chem. Phys., 22, 12 055–12 075, https://doi.org/10.5194/acp-22-12055-2022.

Phillips, V. T. J., J.-I. Yano, and A. Khain, 2017: Ice multiplication by breakup in ice–ice collisions. Part I: Theoretical formulation. J. Atmos. Sci., 74, 1705–1719, https://doi.org/10.1175/JAS-D-16-0224.1.

} } , S. Patade, J. Gutierrez, and A. Bansemer, 2018: Secondary ice production by fragmentation of freezing drops: Formulation and theory. J. Atmos. Sci., 75, 3031–3070, https://doi.org/10.1175/JAS-D-17-0190.1.

} } , J.-I. Yano, A. Deshmukh, and D. Waman, 2021: Comment on "Review of experimental studies of secondary ice production" by Korolev and Leisner (2020). Atmos. Chem. Phys., 21, 11 941–11 953, https://doi.org/10.5194/acp-21-11941-2021.

Reimel, K. J., and M. Kumjian, 2021: Evaluation of k_{dp} estimation algorithm performance in rain using a known-truth framework. J. Atmos. Oceanic Technol., 38, 587–605, https://doi.org/10.1175/JTECH-D-20-0060.1.

Ryzhkov, A. V., 2007: The impact of beam broadening on the quality of radar polarimetric data. J. Atmos. Oceanic Technol., 24, 729–744, https://doi.org/10.1175/JTECH2003.1.

} } , and D. Zrnić, 1998: Beamwidth effects on the differential phase measurements of rain. J. Atmos. Oceanic Technol., 15, 624–634, https://doi.org/10.1175/1520-0426(1998)015,0624:BEOTDP.2.0.CO;2.

} } , and } } , 2019: Radar Polarimetry for Weather Observations. Springer, 486 pp.

} } , } } , and B. A. Gordon, 1998: Polarimetric method for ice water content determination. J. Appl. Meteor. Climatol., 37, 125–134, https://doi.org/10.1175/1520-0450(1998)037,0125:PMFIWC.2.0.CO;2.

} } , T. J. Schuur, D. W. Burgess, P. L. Heinselman, S. E. Giangrande, and D. S. Zrnic, 2005: The Joint Polarization Experiment: Polarimetric rainfall measurements and hydrometeor classification. Bull. Amer. Meteor. Soc., 86, 809–824, https://doi.org/10.1175/BAMS-86-6-809.

} } , M. Pinsky, A. Pokrovsky, and A. Khain, 2011: Polarimetric radar observation operator for a cloud model with spectral

bin microphysics. J. Appl. Meteor. Climatol., 50, 873–894, https://doi.org/10.1175/2010JAMC2363.1.

} } , P. Zhang, H. Reeves, M. Kumjian, T. Tschallener, S. Tromel, and C. Simmer, 2016: Quasi-vertical profiles}A new way to look at polarimetric radar data. J. Atmos. Oceanic Technol., 33, 551–562, https://doi.org/10.1175/JTECH-D-15-0020.1.

Schaefer, V. J., and R. J. Cheng, 1971: The production of ice crys-tal fragments by sublimation and electrification. J. Rech. Atmos., 5, 5–10,

Sinclair, V. A., D. Moisseev, and A. von Lerber, 2016: How dual-polarization radar observations can be used to verify model representation of secondary ice. J. Geophys. Res. Atmos., 121, 10 954–10 970, https://doi.org/10.1002/2016JD025381.

Tobin, D. M., and M. R. Kumjian, 2017: Polarimetric radar and surface-based precipitation-type observations of ice pellet to freezing rain transitions. Wea. Forecasting, 32, 2065–2082, https://doi.org/10.1175/WAF-D-17-0054.1.

Tyynelä, J., J. Leinonen, D. Moisseev, and T. Nousiainen, 2011: Radar backscattering from snowflakes: Comparison of fractal, aggregate, and soft spheroid models. J. Atmos. Oceanic Technol., 28, 1365–1372, https://doi.org/10.1175/JTECH-D-11-00004.1.

Vulpiani, G., M. Montopoli, L. D. Passeri, A. G. Gioia, P. Giordano, and F. S. Marzano, 2012: On the use of dual-polarized C-band radar for operational rainfall retrieval in mountainous areas. J. Appl. Meteor. Climatol., 51, 405–425, https://doi.org/10.1175/JAMC-D-10-05024.1.

} } , L. Baldini, and N. Roberto, 2015: Characterization of Mediterranean hail-bearing storms using an operational polarimetric X-band radar. Atmos. Meas. Tech., 8, 4681–4698, https://doi.org/10.5194/amt-8-4681-2015.

Zawadzki, I., F. Fabry, and W. Szyrmer, 2001: Observations of supercooled water and secondary ice generation by a vertically pointing X-band Doppler radar. Atmos. Res., 59–60, 343–359, https://doi.org/10.1016/S0169-8095(01)00124-7.

Zhao, M., and Coauthors, 2016: Uncertainty in model climate sensitivity traced to representations of cumulus precipitation microphysics. J. Climate, 29, 543–560, https://doi.org/10.1175/JCLI-D-15-0191.1.